Extreme Metamaterial Solar Sails for Breakthrough Space Exploration
NIAC Phase II report

PI: Artur Davoyan[1]
Co-Is: Henry Helvajian[2], Les Johnson[3], Marko Velli[1]

[1]*University of California Los Angeles*
[2]*The Aerospace Corporation*
[3]*NASA Marshall Space Flight Center*
davoyan@seas.ucla.edu

Abstract: The past 60 years of space exploration have led to fascinating discoveries across many different branches of science and technology. However, further progress requires new revolutionary approaches to in-space propulsion for fast transit across the solar system and beyond. Here, we describe the concept of extreme solar sailing, in which we show by making use of a powered slingshot at extreme proximity to the surface of the sun, <5 solar radii, solar sails can be accelerated to >60 AU/yr (>300 km/s or 0.1% speed of light). We discuss associated materials challenges, environmental issues, sailcraft architecture and controls. We further analyze two mission concepts – Fast Transit Interstellar Probe and a precursor Corona-Net mission. We show that with proper technology development, such extreme solar sailing is feasible in the near term and can significantly transform the way space is explored today. If available, such solar sailing technology would allow fast flight through the solar system and at arbitrary inclinations to the plane of the ecliptic. A flight to Jupiter would take 5 months, 10 months to Neptune, Voyager 1 will be surpassed in 2.5 years, and 1000 AU reached in 17 years.

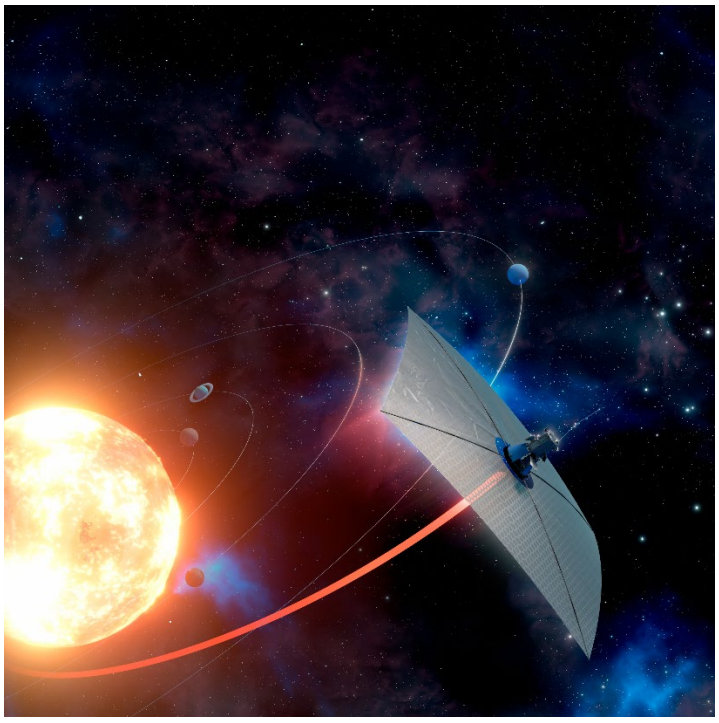

By sailing in extreme proximity to the sun (2-5R☼), solar sails can be propelled to over 60 AU/year.

Table of Contents

I. Introduction

Space exploration paves the way to fascinating discoveries that elucidate the makings of our solar system and of the sun, and more recently also shedding "light" on the early days of the universe itself. Despite the tremendous successes of past decades, present-day close-up space exploration is hindered by the limitations of existing spacecraft technologies, which are fundamentally constrained by the rocket equation. Chemical and electrical propulsion systems that are in use today are slow. Moreover, they have led to costly missions. Indeed, a wide range of envisaged destinations and orbits are inaccessible to present-day spacecraft. Flagship-type missions take years of development, with price tags frequently exceeding $1B. For example, the outer planets beyond Saturn have been visited only once (Fig. 1), whereas only two probes have left the solar system to date [1] (Fig. 2). It took Voyager 1 cruising at an unbeaten speed record of 3.6 AU/year (17 km/s) 35 years to reach the heliopause. Exploration of the Sun is likewise constrained by the limitations of the existing propulsion systems [2]. Reaching high solar latitudes and polar regions, especially in the solar corona and inner heliosphere, is an insurmountable task at present**. Future discoveries call for a paradigm shift in propulsion and spacecraft design that is coupled with a new concept of operations (CONOPS) that will enable faster, cheaper, and massively scalable ubiquitous exploration of the solar system and beyond. <u>We envisage extreme solar sailing is the technology that can lead this transformative leap.</u>**

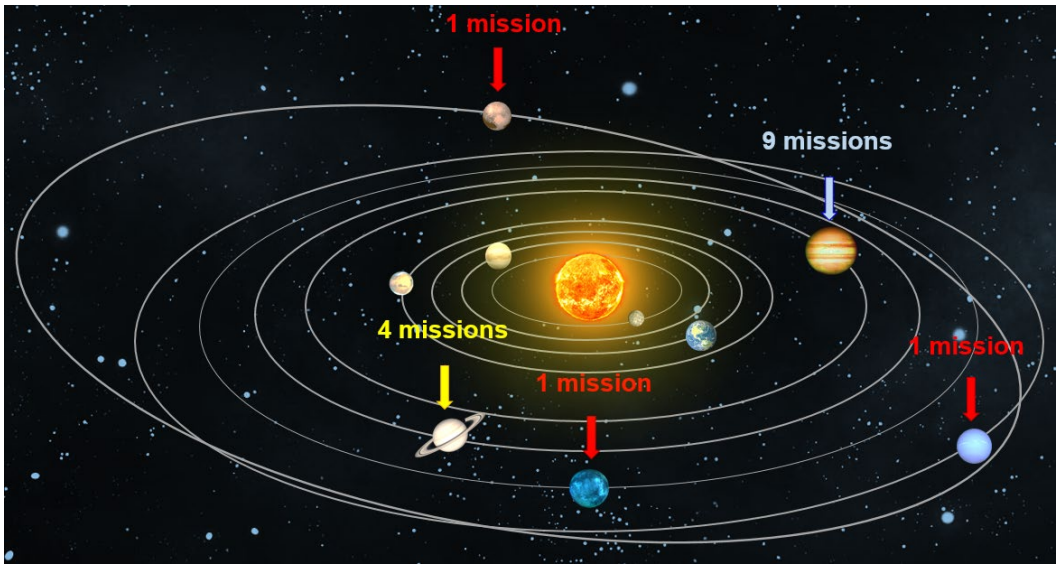

Fig. 1*. Schematic illustration of the solar system with a number of missions to outer planets indicated. Planets beyond Saturn have been visited only once throughout the entire history of space exploration.*

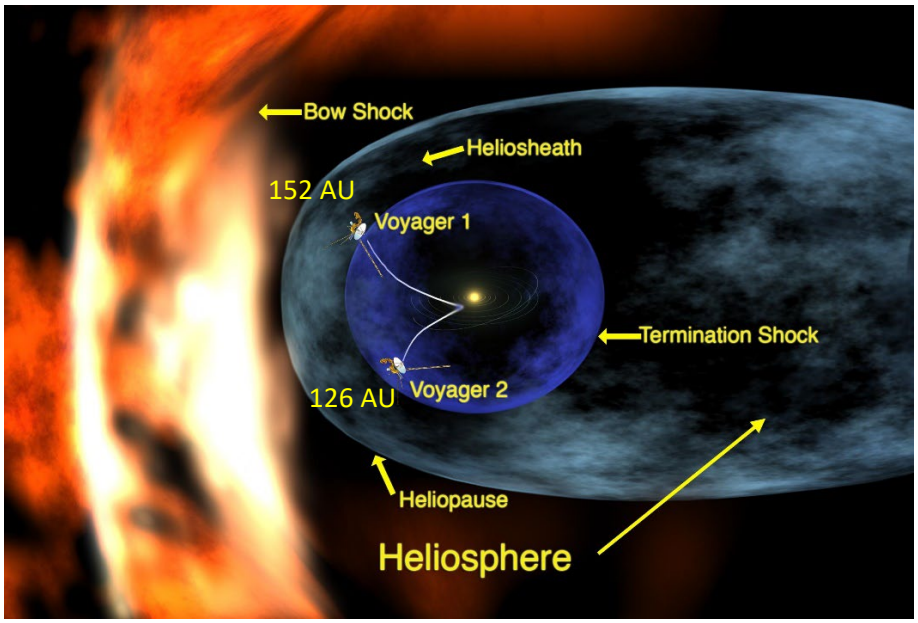

Fig. 2. *Artistic illustration of the heliosphere and interstellar medium (credit: NASA/JPL). Only two probes – Voyager 1 and Voyager 2 – have reached the heliopause to date. It took Voyager 1 cruising at a record-breaking speed of 3.6AU/year 35 years to reach this milestone.*

Solar sail propulsion is traditionally viewed as a slow and cumbersome alternative to electric rockets having a relatively narrow niche for science missions. Hardly anyone can imagine a major solar sail mission to Europa or Titan. Nevertheless, solar sails, owing to a **fundamentally different propulsion physics which is based on light radiation pressure, have the ability to reach unprecedented velocities and orbits** [2-16] (e.g., solar poles or out of ecliptic) that are inaccessible by electric or chemical rockets. The advantage of solar sailing is particularly manifested in maneuvers within Mercury's orbit and *closer to the sun*, where the radiation pressure is strong. For example, orbits with arbitrary inclinations to the plane of the ecliptic and arbitrarily close perihelia may be easily and quickly reached, provided that proper materials and architecture exist. Lightweight solar sails have the potential to open a new chapter for space exploration with a particular promise for fast solar system exploration and interstellar flight. In particular, by performing a powered slingshot maneuver (i.e., Oberth maneuver) in close proximity to the sun (Fig. 3 (left)), lightweight solar sails may be accelerated to unprecedented velocities. In Fig. 3 (right), we plot calculated heliocentric exit velocity with perihelion distance for different sail areas to an overall spacecraft mass ratio, A/m (we use sail area to total spacecraft mass ratio (i.e., including mass of the sail, mass of corresponding support system, and mass of the spacecraft bus) as our figure of merit; other metrics may include characteristic acceleration and sail loading, which are directly related to A/m used in this work). By making a close perihelion, <6R$_\odot$ (Parker Solar probe's nearest approach is ~9R$_\odot$ [17]) slingshot maneuver, solar sails can propel a lightweight spacecraft (~10-20 kg) to velocities above 60 AU/year (>300 km/s). These velocities are well above that of other technologically feasible proposals recently considered [18-21], including solar thermal rocket (~22 AU/year), SLS class rocket with Jupiter and solar gravity assists (<15 AU/year), nuclear electric propulsion (~20 AU/year), and electric sailing (12-23 AU/year). Beamed energy propulsion, while capable of accelerating a spacecraft to even higher velocities [22-31], is limited by very low payload mass and the significant infrastructure challenges associated with the beam forming technology (e.g., Starshot initiative suggests the use of 1 km^2

100 GW laser array to propel a 1g spacecraft to 20% of the speed of light [30, 31]). Fusion and antimatter propulsion are the two other technologies proposed [32-35] for fast transit high delta-V missions. However, these technologies require further foundational physics breakthroughs. Compared to these alternatives, extreme solar sailing, as shown in Fig. 3 (left), puts forth the promise for a set of exploration approaches and science missions that are enabled by fast transit time (planetary and interstellar) and novel solar monitoring probes. A flight to Jupiter would take 5 months, 10 months to Neptune, Voyager 1 will be surpassed in 2.5 years, and the solar gravity lens location [36] (550 AU) reached in just 8.5 years!

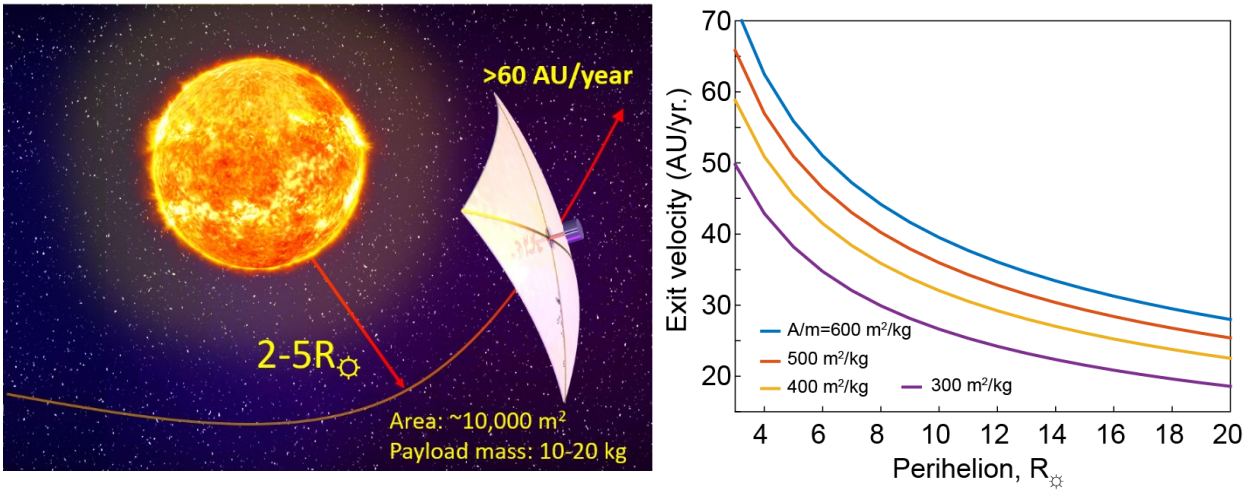

Fig. 3. *(left) Conceptual illustration of the slingshot maneuver. (right) A calculated sailcraft heliocentric excess velocity (i.e., solar system exit or cruise velocity) with perihelion distance for different sail area to spacecraft mass ratios. Here, an ideal, flat, perfectly reflecting sail is assumed. For details of the calculation, see Sec. IV. We note that our estimates are on the conservative side, and other sail exit velocity calculations [36] provide even higher values.*

With the maturation of solar sail propulsion, we envisage new missions emerging, all driven by the proliferation of small satellite technology, further miniaturization of instrumentation, and the substantial decrease of launch costs. Imagine cost-effective (~$10M total) deep space missions that rely on small 10 – 50 kg spacecraft. The sailcraft would start their journey from Earth orbits and quickly reach anywhere in the solar system, even out of the ecliptic plane, Fig. 4, ***effectively turning our sun into a launch pad***. While sailcraft may not directly replace present-day large utility flagship planetary missions, given mass production know-how and its derived economy of scales, the sailcraft approach provides more frequent data taken from different perspectives than current flagship mission craft can ever do.

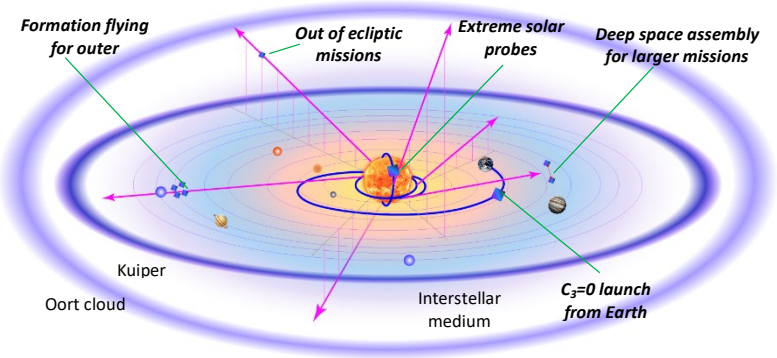

Fig. 4. Sun as a launch pad*: By spiraling in and within "touching" distance to the Sun (< 6R☼), multiple low-cost sailcraft may be placed on arbitrary exit trajectories and high inclination orbits in the solar system and beyond.*

Moreover, by applying in-space assembly and docking technology to sailcraft, the formation of larger mission-adept structures can be assembled during a transit phase, which can compete with present-day flagship missions. For example, the assembly of a 1-ton spacecraft (e.g., comparable to Perseverance rover) traveling at 60 AU/year would require aggregation of ~50 sailcraft.

II. Concept of operations

We begin our discussion with a brief outline of the concept of operations for extreme solar sailing missions. Fig. 5 shows a conceptual illustration of an extreme solar sailing mission.

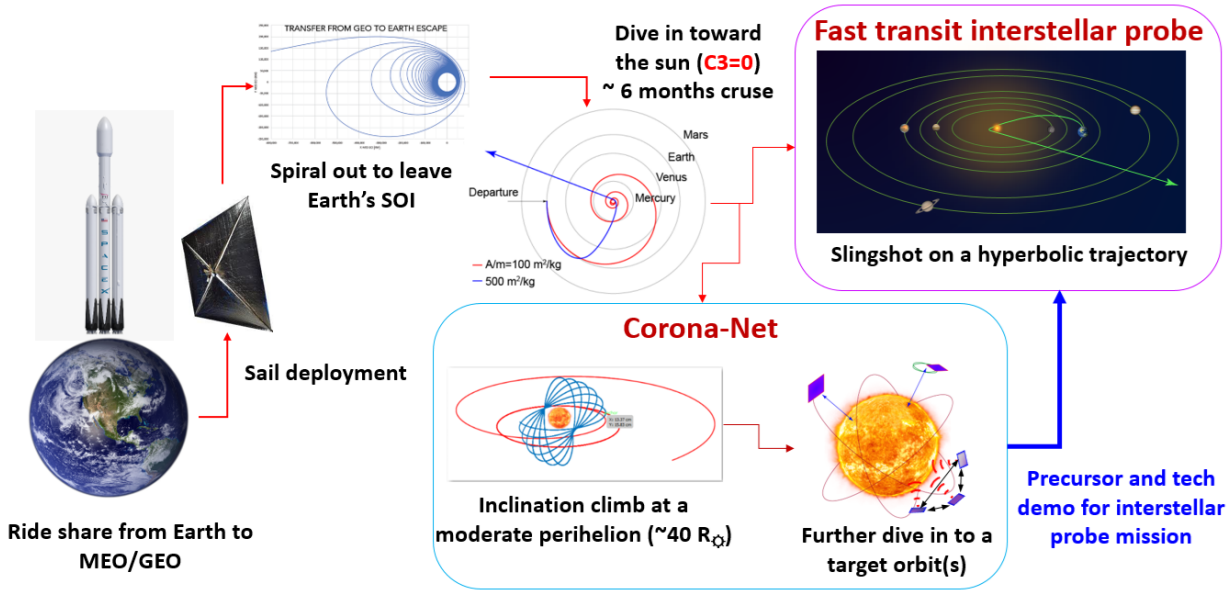

Fig. 5. Conceptual illustration of the extreme solar sailing concept of operations.

Stage 1: Solar sail launch and deployment. At this stage, a solar sail spacecraft is launched into a desired Earth orbit. Higher altitude orbits are preferable. Once in orbit, a sail is deployed. Note that sail deployment was flight-tested by several previous missions. Importantly, this stage does not require a dedicated launch vehicle. Hence, a solar sail spacecraft may be launched as a secondary payload, in which case launch costs can be drastically minimized.

Stage 2: Leaving the Earth's sphere of influence. Once in orbit, the sailcraft performs a set of maneuvers to leave the Earth's orbit. A recent flight test of LightSail 2 validates that technologies necessary to accomplish this maneuver exist. Such solar sail spacecraft will slowly spiral out toward the edge of the Earth's sphere of influence and enter the interplanetary medium. The duration of this maneuver depends on the starting altitude and may take several months, depending on the sail area to mass ratio. The sail will then leave the sphere of influence with near-zero inclination to the plane of the ecliptic and $c_3 \simeq 0 \frac{m^2}{s^2}$ target parameter (i.e., in a heliocentric reference system, we may assume that the initial sail velocity is 29.78 km/s). Note that faster orbital insertion may be possible with secondary payload on interplanetary missions.

Stage 3: Spiraling in toward the sun. Once in interplanetary space, sail motion is fully governed by the solar gravitation attraction and solar radiation pressure. At first, the sail is brought close to the sun. For this purpose, the sail is oriented at an angle with respect to the sunline (i.e., at an angle with respect to incident radiation). The duration of this stage depends on the sail area to mass ratio

(or, equivalently, its characteristic acceleration). Hence, it takes ~152 days for lighter spacecraft (i.e., with $\frac{A}{m}$ = 500 m^2/kg) to reach perihelion, and ~270 days for the $\frac{A}{m}$= 100 m^2/kg spacecraft, respectively.

Stage 4: Orbit selection and sail insertion. Once a desired minimum distance from the sun is reached, the spacecraft performs maneuvering depending on overall mission objectives. Here, several conceptually different mission opportunities exist. Staying in the vicinity of the sun allows for probing heliophysics, including at very high inclination orbits. Meanwhile, performing an Oberth-like maneuver at a very small perihelion allows injecting a sailcraft onto fast exit trajectories for the outer planets and interstellar missions.

In Phase II we have briefly considered two mission concepts of interest:

- **Fast Transit Interstellar Probe** – a solar sail mission that aims to reach 500 AU in less than 10 years. The mission's primary objectives are to understand and map properties of local and pristine interstellar medium. Several of such probes will enable mapping the anisotropy of the heliosphere and measuring composition and parameters of the interstellar medium across different directions, including out-of-the-ecliptic (e.g., along the sun pole direction). The mission concept will also enable multiple other missions, including:
  - Fast and regular flyby missions to outer planets/moons and Trans-Neptunian objects. For example, with a formation-flying of 3-5 spacecraft, outer solar system celestial bodies may be imaged and characterized from several vantage points.
  - Search for Planet Nine and/or blackholes in the solar system
- **Corona-Net mission concept** – a solar sail mission that aims at placing a formation-flying of several sailcrafts at high solar latitudes of $< 5R_{\odot}$. The primary goal of the Corona-Net mission is to bring important high-resolution spatio-temporal data about the inner corona, thus helping to answer long-standing major open questions about the solar magnetic field, accretion of the solar wind, and solar dynamo. Corona-Net poses less stringent criteria for craft design (i.e., can be performed with a smaller area-to-mass ratio ($\frac{A}{m}$~50-100 m^2/kg)). As such, the ***Corona-Net mission also serves as a precursor mission*** for the Fast Transit Interstellar Probe mission concept.

III. Science objectives

A small CubeSat-size spacecraft powered by solar sails can reach orbits and destinations that are inaccessible by current probes. As such, new opportunities for studying the physics of the sun, solar wind interaction with planetary magnetospheres, heliosphere, and beyond emerge. In Ref. [37], we have outlined science cases that can be addressed by such fast-transit solar sail spacecraft.

III.1. Understanding the physics of the sun. Understanding the detailed dynamics of the magnetically active sun is of paramount importance for predicting the space weather and shedding light on the formation of our solar system. While studies of the sun and heliosphere play a central role for NASA and other agencies, a number of grand questions remain open.

The origin and dynamics of the solar dynamo, with its unpredictable extreme minima and maxima, the evolution of magnetic fields, and their connection to coronal heating and solar wind acceleration, are yet to be explained in terms of first principles. The recently launched Parker Solar Probe and ESA's Solar Orbiter provide important observations, revealing the physics of magnetic

fields at small – hundreds of kilometer - scales. Ubiquitous reconnection at the base of the solar corona appears to be at the heart of the generation of the solar wind. The omnipresence of large amplitude magnetic field fluctuations with incorporated switchback, s-like reversals, propagating outwards provides supplementary solar wind heating and acceleration. These missions suggest the importance of continued *in-situ* observations close to the sun. The role of the overall magnetic topology in generating different solar wind types and different types of energetic eruptions suggests that the full 3D geometry of the solar field and its time dependence in the vicinity of the sun need to be measured and understood. While low-resolution maps below ~ 50^o solar latitude can be inferred from terrestrial and space-borne observations (Fig. 6), studies above 50^o, especially in the inner corona, are not possible via any present-day spacecraft. On the other hand, consistent space weather prediction requires quasi-contemporaneous measurements of the magnetic field over the full 4π solid angle. The solar sails equipped with a suite of local antenna and magnetometer probes could be the first to reveal spatio-temporal dynamics of the magnetic field at high solar latitudes, with its turbulent dynamical properties. Potential future extension of our spacecraft to include other instruments, such as particle detectors and, possibly, imaging spectrometers, would yield multi-messenger observations of the sun.

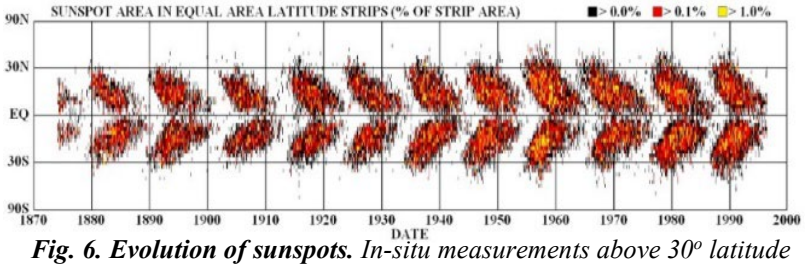

Fig. 6. Evolution of sunspots. *In-situ measurements above 30^o latitude are key to understanding the sun.*

III.2. Probing heliosphere and interstellar medium. Solar wind interaction with the interstellar medium creates a bubble-like plasma region – the heliosphere – around the sun, Fig. 7. The importance of the heliosphere for life can't be understated as it shields planetary systems from cosmic radiation. A detailed understanding of the solar wind and solar magnetic field interaction with interstellar plasmas could also serve as a proxy for understanding and refining habitability conditions for exoplanets. With data obtained by Voyagers and New Horizons and new simulation models, standard views on the shape of the heliosphere bubble have been revised. Specifically, it is believed that the heliosphere shape drastically differs from the conventionally accepted one (shown in Fig. 7). However, exploration of the heliosphere is challenged by vast distances (~100 AU). Solar sails capable of traveling>25 AU/year, including out of the ecliptic plane, could quickly reach the heliopause in different directions, bringing new data about the terminal shock, solar wind – interstellar medium interaction, and solar wind influencing on local interstellar medium. With the low cost of solar sail missions, multiple probes

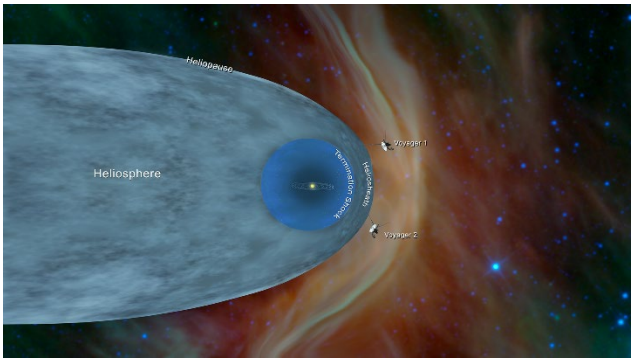

Fig. 7. Artistic illustration of the heliosphere according to traditional views. *Multiple sailcarft could probe the shape of the heliosphere and reveal details of solar wind interaction with interstellar medium.*

can be sent in different directions allowing to probe anisotropy of the heliosphere and resolving ongoing debate on the shape of the heliosphere bubble.

Beyond heliopause lies interstellar medium. Only two probes – Voyagers 1 and 2 – have reached the local interstellar medium, Fig. 7. At the same time, only the transition region has been investigated so far. At distances >500 AU lies pristine local interstellar medium. At present our understanding of local interstellar medium is based on measuring optical absorption measurements of light emitted by nearby stars. The data shows that our solar system may be at the boundary of two interstellar clouds (G Cloud and Local Interstellar Cloud). In situ measurements could yield a more detailed picture of the properties of the transition region, as well as the structure and composition of the interstellar clouds. This is where fast transit probes traveling at >50 AU/year could allow probing pristine interstellar medium in the local neighborhood.

IV. Sail materials

Our analysis of the environment in the vicinity of the sun (~5R☼ from the surface) (see Sec. VI) shows that solar radiation (i.e., black body emission of electromagnetic waves) is the dominant factor that dictates the material choice and design (other factors include solar wind plasma, coronal mass ejections, solar flares, interplanetary dust, and solar energetic particles).

Sun is continuously emitting electromagnetic radiation as a black body at ~5770 K. The spectrum of this radiation in space at Earth orbit is known as the Air Mass Zero (AM0) spectrum. And the overall irradiance at Earth orbit is ~1367 W/m^2. The intensity of radiation varies inversely proportional to the distance square, and at ~ 5R☼, it reaches >1500 times that of Earth. As such, sail materials and structures that can withstand such high heat flux are needed. At the same time, sail material must be very lightweight (<2 g/m^2). With radiative heat rejection being the only mechanism for heat management in space, such sail materials need to be carefully engineered to exhibit high backside thermal emissivity, low front-side solar absorptivity, operate at elevated temperatures (>1000 K), as well as be great reflectors to maintain high radiation pressure force. In Phase I, we have surveyed a range of high-temperature materials. We showed that TiN and SiN films may make great candidates for solar sail materials design. In Phase II, we have prototyped a range of samples.

IV.1. TiN-based sails.

TiN is a high-temperature ceramic exhibiting metallic properties. A metamaterial design based on TiN is reminiscent of the currently used aluminized polyimide sails. Specifically, a TiN-based sail comprises a ~80 nm thick TiN film that is deposited atop a sub-micron thick inorganic high-temperature film which acts as a substrate (e.g., graphene composites, carbon nanotubes (CNT) or boron nitrite composites, as shown Fig. 8. TiN-

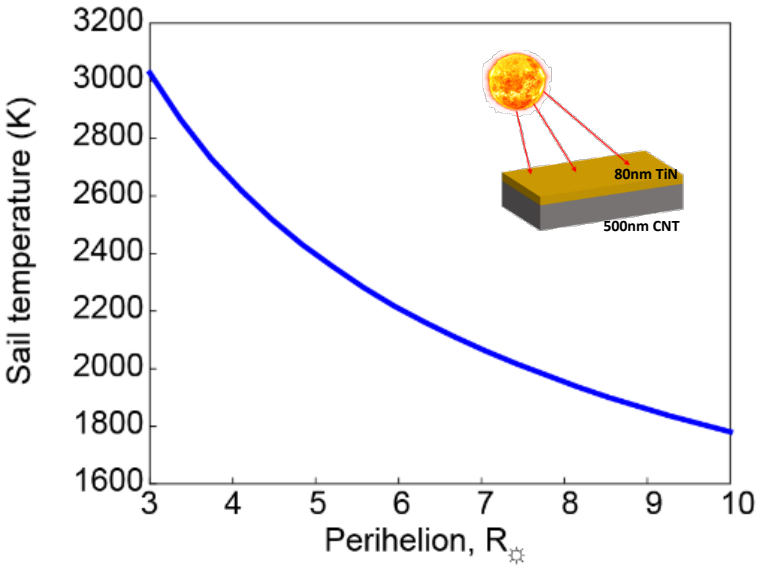

Fig. 8. *TiN based solar sail. Sail temperature with perihelion distance. Inset shows sail schematic. Melting point of TiN is 3200 K*

based sails would reflect about 60% of sunlight and absorb the other 40%. This corresponds to 80% efficiency for momentum transfer under normal incidence as compared to an ideal flat perfectly reflecting sail. To control the temperature rise and prevent overheating, the backside of the substrate is coated with a thin thermally emissive surface that functions to cool by radiative means. For example, a 500-nm thick CNT film is expected to have an emissivity of $\epsilon \simeq 0.7$ at $T \geq 1800\ K$, which can be further enhanced by depositing a few nm of tungsten (W) (being metallic in nature, sun-facing TiN surface has very small emissivity $\epsilon \leq 0.05$). Our calculations indicate that such films may get up to 3R☼ perihelion before reaching a melting temperature of 3200 K (Fig. 8). Such a sail with an areal density $\leq 0.7\ g/m^2$ is capable of propelling a 20-kg bus (i.e., excluding sail systems) to ~60 AU/year.

To prototype such a sail design, we have developed a fabrication process to create thin, free-standing TiN/CNT composites. Fig. 9 shows a photograph of one of the films. Here, a fabricated film is made of an 80 nm thick TiN coated atop a ~ 1 um thick multi-wall carbon nanotube film.

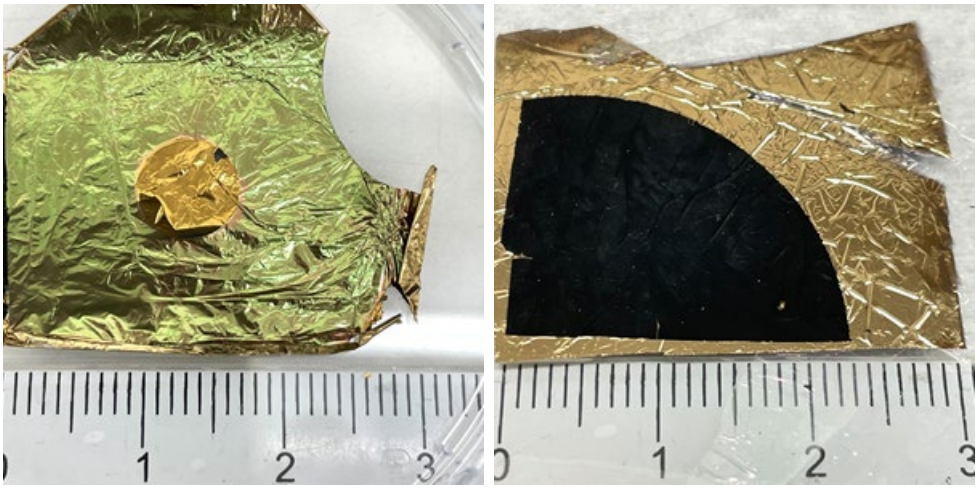

Fig. 9. Prototyped TiN-based solar sails membranes. *Front (left) and backside (right) of the titanium nitride-coated MWCNT film. The circle in the middle is the free-standing part.*

In addition to TiN sail samples, we also have prototyped sail materials with other metal films, including Al-based and Pt-based. In both cases, removing the underlying low-temperature polyimide film allows operating at elevated temperatures (limited by the metal degradation). These sails can get closer to the sun than conventional solar sail materials. Figure 10 shows a photographic image of a Pt/CNT-based sail membrane. Here, again, ~100 nm Pt film is deposited atop ~ 1 micron thick CNT film. Notably, the film has good optical properties comparable to that of a Pt film deposited atop a solid smooth substrate. Related spectral measurements show a good match with theoretical models (Fig. 10 (left)). In particular, we observe that fabricated Pt samples reflect over 70% of sunlight across the visible frequency range.

Figure 11 shows fabricated Al/CNT sail membranes. CNT thickness is again ~ 1 um thick, suggesting that the overall areal density of the fabricated membrane is <0.5 g/m^2. However, fabricated samples are rather gentle and easily tear when small forces are applied (as seen in the case of Pt, Fig. 10). Thermal tests on Al/CNT samples conducted in an ambient atmosphere show that samples withstand a heat load of 450 ºC, when placed on a hot plate. This operation

temperature is higher than that for conventional sail materials. Related measurements of reflectivity do not reveal a significant drop in functionality.

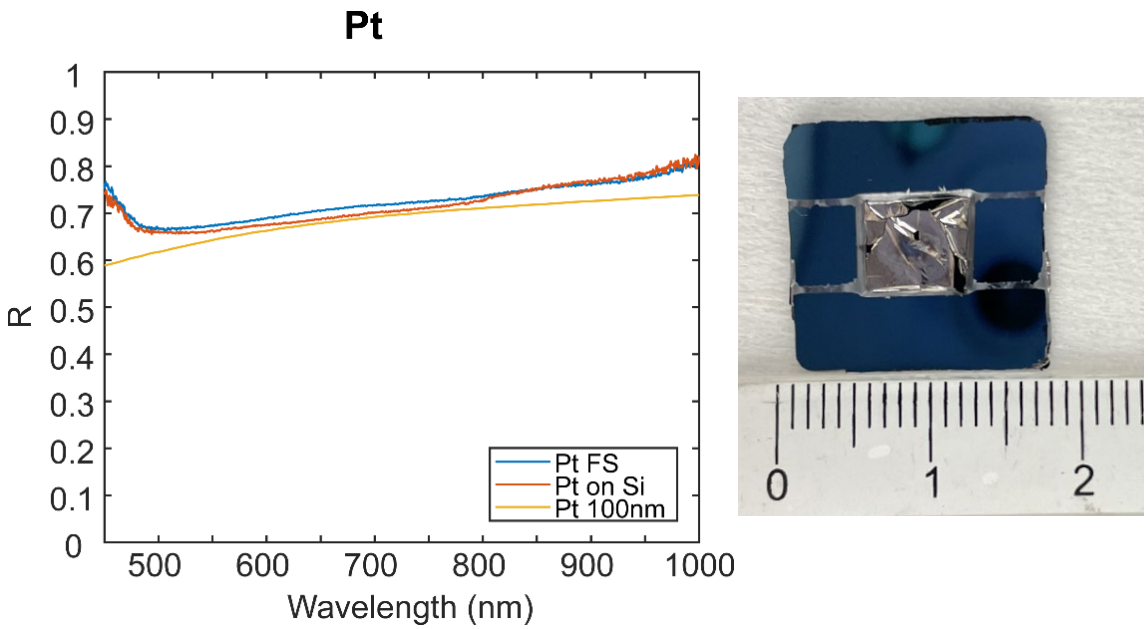

Fig. 10. *(Left) Reflectivity of solar sail material sample with Pt reflection layer, compared with reference sample and theoretical curve. (Right) Photograph of the fabricated Pt-MWCNT solar sail sample suspended on silicon frame.*

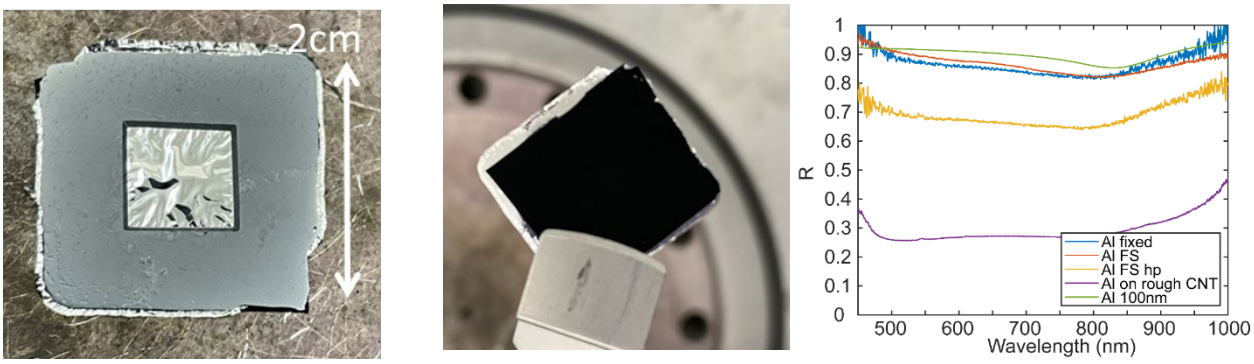

Fig. 11*. Front (left) and back (middle) side photos of free-standing solar sail samples suspending on silicon frames. (right) Reflectivity of aluminum-coated solar sail material samples before and after heat treatment, compared to theoretical curve, a reference sample, and aluminum directly deposited onto MWCNT films.*

IV.2. SiN-based sails.

SiN presents a conceptually different alternative to metamaterial sail design. Thin SiN-based films absorb sunlight only weakly ($\leq 0.1\%$). With proper emissivity control, the combination permits maintaining relatively low temperatures ($\sim 1600\,K$) even at very close perihelion

distances ($< 3R_{\odot}$ from the surface of the sun). However, SiN, being naturally transparent, reflects only a fraction of the sunlight and consequently is not efficient for momentum transfer and adequate creation of propulsive thrust. To boost the reflectivity of SiN and enhance radiation pressure momentum transfer, we investigated nanostructured metamaterials that are made of SiN.

Utilizing Particle Swarm optimization, we first examined a multilayer sail material architecture (Fig. 12). The result of such optimization for a low-loss silicon nitride is shown in Table 1. Figure 12 shows an example of an optimized 7-layer structure and a related reflectance spectrum.

Table 1. Optimization results for multilayer sails using low-loss silicon nitride data

	5 layers	**7 layers**	**11 layers**	**15 layers**
Reflectivity	0.5679	0.6562	0.7659	0.8357
Absorptivity	3.5438e-04	4.3566e-04	7.8678e-04	0.0013
Emissivity	0.0705	0.0949	0.1637	0.1502
Perihelion distance ($R_{\odot}$)	< 1	< 1	< 1	< 1
Sail temperature (K)	951.9038	929.4589 K	940.6814	1114.6
Areal density (g/m^2)	0.9494	1.4145	4.5016	6.8215

According to the table, optimization clearly shows improvement in reflectivity as compared to conventional Bragg reflectors. Adding more layers helps improve reflectivity even further (e.g., 11-layer structures yield reflectivity as high as 70%), however, at the cost of increased areal density. For low-loss SiN, all of the designs can reach <2 $R_{\odot}$ from the surface of the sun and maintain a reasonable sail temperature.

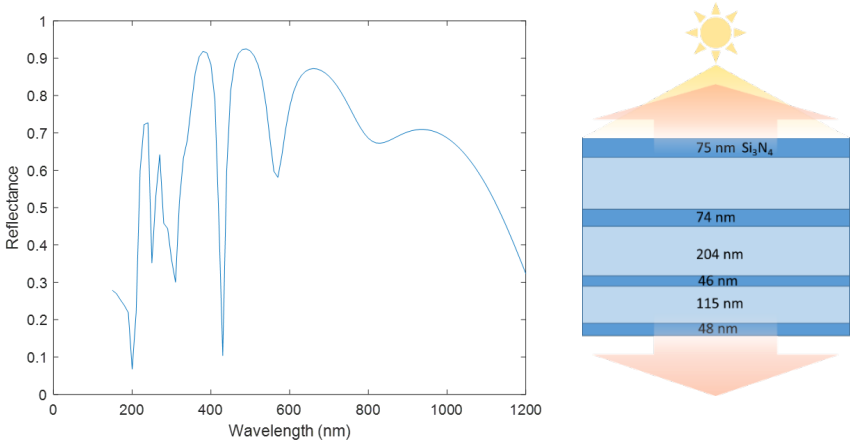

Fig. 12*. The reflectance of a 7-layer design optimized by PSO. A broad reflection band can be achieved by multilayer design.*

More complex metamaterial structures can yield even better performance. Fig. 13 shows an example of a more elaborate design. In this case, we obtain >60% solar reflectivity and areal density <1 g/m^2. Such sail materials allow for high area-to-mass ratio sails and can reach very small perihelion distances (<2 R☼). Use of such sail materials on future solar sail missions could enable very high exit velocity missions, with a velocity >50 AU/year.

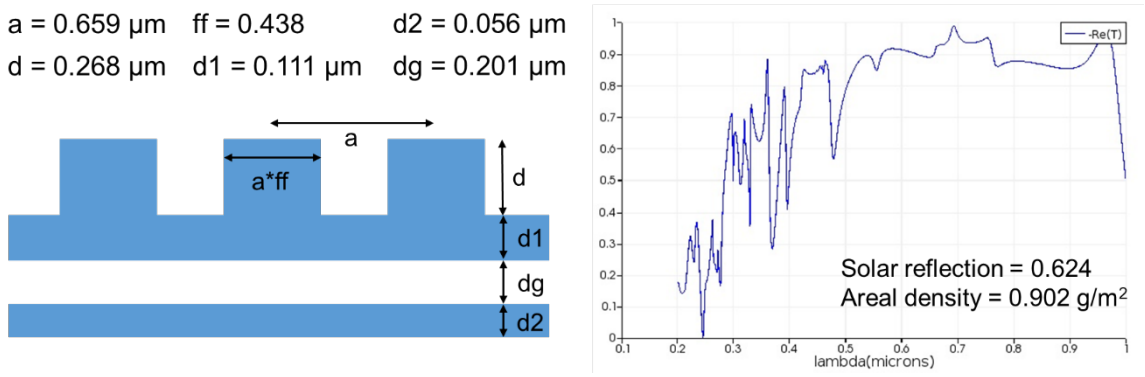

Fig. 13. *Optimization of a SiN sail.*

While SiN metamaterial fabrication is more elaborate, the lower temperature of such metamaterial presents a more attractive approach than TiN.

V. Solar environment

Together with accounting for solar radiation absorption and respective thermal balance, it is important to understand the environment of the corona in close proximity to the sun to determine key challenges and damaging mechanisms that sail materials and sail systems (e.g., controls) will face. We can conceptually divide all of the environmental effects outside of >3R☼ into two main categories: "steady state effects" and "transients."

V.1. Steady state effects.

Steady-state effects are solar effects that are present at all times, can be empirically modeled and predicted, and vary relatively slowly (as compared to sail controls and/or mission duration). Steady-state effects include solar radiation, solar wind, dust, average solar magnetic field, continuous average background flux of energetic particles, and photons.

Solar wind. Numerous observations of the corona in visible and radio parts of the spectrum, as well as many missions, launched to study the solar wind and magnetosphere (e.g., Parker Solar Probe, SOHO, ESA's Solar Orbiter), provide reliable empirical models that help understand key parameters of the solar wind plasma in vicinity of the sun. In Table 2, we provide a brief summary.

Table 2. Key solar wind parameters.

Physical property	Value
Composition	95% protons, ~5% - He+, trace amount of heavier elements
Wind velocity	200 km/s – 800 km/s • speed depends on solar latitude, solar surface activity (faster above sun spots), perihelion distance (speed is lower in the vicinity of the sun) • solar wind speed at ~3-5R☼ is >2x smaller than at >10R☼ • solar wind contains slow (200 km/s-400 km/s) and fast (700 km/s-800 km/s) components • the velocity may reach up to 2000 km/s (at >10R☼) during a major solar wind disturbance event (e.g., coronal mass ejections)
Wind temperature	10^6 K–10^7 K ($\leq 1\ keV$) at 3R☼–10R☼ • drops as ~1/r beyond 10R☼ • wind plasma temperature is not to be mixed with the sail temperature
Carrier density	10^5 cm^{-3}-10^6 cm^{-3} at 3R☼ ~10^4 cm^{-3} at 5R☼ • depends on solar activities • is several times higher during a major solar wind disturbance event • drops as ~$1/r^2$ for r > 10R☼
Magnetic field	up to 10 μT at 3R☼ (drops as ~$r^{-1.5}$) – compared with Earth's magnetic field of ~60 μT at poles

The relatively small density of the solar wind plasma, even at 3R☼, suggests that solar wind plays a secondary role in sail materials damage compared to solar electromagnetic radiation. To assess the effects of solar wind damage, we have conducted a set of Monte Carlo simulations using Stopping Range of Ions in Matter (SRIM) software. Figure 14 illustrates the simulation setup and an example result of ion-target interaction. Here, we simulate 100 nm aluminum – 100 nm CNT as a prototype solar sail. Hydrogen ions are injected into the thin film with the energy calculated from the solar wind proton temperature, along with the energy gained from falling through the sheath potential. In the example in Fig. 14, the injected hydrogen ion energy is 419 eV from the solar wind proton energy at 5 $R_☼$ without considering the sheath effect. The thin red lines indicated the trajectory of the ions once injected into the material.

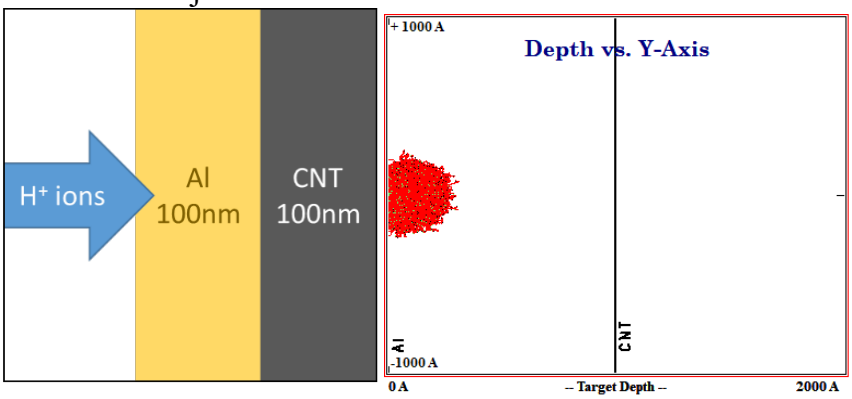

Fig. 14. *(left) diagram showing the TRIM setup (right) cross-section plot of collision between ion and target material.*

The output of the TRIM simulation is the number of sputtered atoms per incident ion. We can then define the sputtering damage rate as:

$$sputtering\ damage\ \left[\frac{cm}{s}\right] = \frac{\frac{\#\ sputtered\ atoms}{\#\ incident\ ions} \times flux\ \left[\frac{\#}{cm^2 \times s}\right]}{atomic\ density\ of material\ \left[\frac{\#}{cm^3}\right]},$$

where solar wind flux is calculated assuming an average solar wind particle velocity of ~416 km/s. Figure 15 shows the resulting sputtering damage rate as a function of distance from the sun's surface. As expected, as the sail approaches the sun, due to the increase of solar wind temperature and plasma density, the sputtering damage increases.

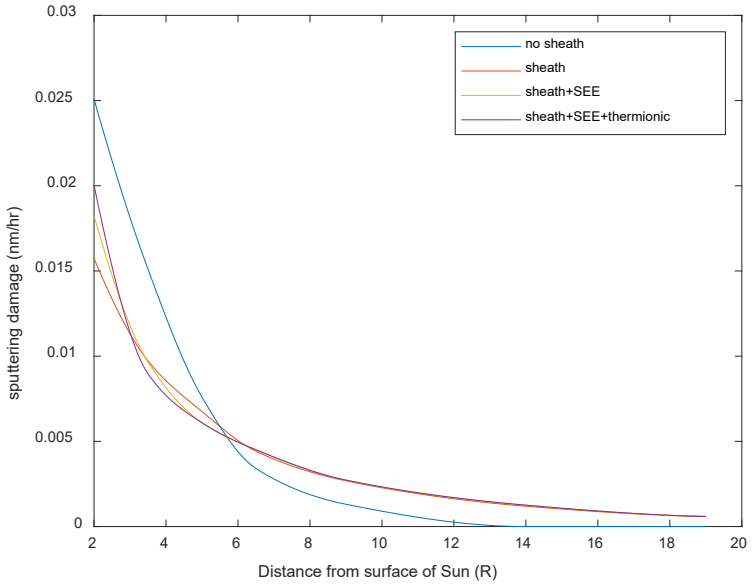

Fig. 15 *Sputtering damage rate with and without account of sheath and secondary electron emission.*

V.2. Transients events.

Transient events include coronal mass ejections, solar flares, and solar energetic particles. These effects depend on the solar activity cycle. While their occurrence and strength are hard to predict, short perihelion transit time allows us to build probabilistic models that may minimize potential exposure. For this purpose, we assess the number of intercepts a spacecraft may experience in case it is in a circular orbit around the sun. We consider a nominal orbit of ~ 3R☼ radius. Fig. 16 shows CME distribution for both solar activity minima and maxima per SOHO data. Based on this data, we then run Monte Carlo simulations to assess the probability of getting into a CME event over 1 year duration on such a circular orbit. We find that in the case of solar maxima, the probability of passing through a CME event is ~12% during 1 year of flight, whereas in the case of solar minima, such a probability is <6%. Additionally, analysis shows that for orbits in the plane of ecliptic the probability of encountering a CME is drastically higher than for polar and high inclination orbits. Based on this analysis, we conclude that solar orbiting missions need to be carefully designed to withstand potential high doses of damaging radiation received during potential CME events. At the same time, for flyby fast transit missions, which spend only a few

days in the vicinity of the sun, the probability of encountering a CME is very small and should be a secondary factor in designing a mission. Of course, a more detailed subsequent study that would assess more precisely the damaging effects of solar radiation on spacecraft components is needed.

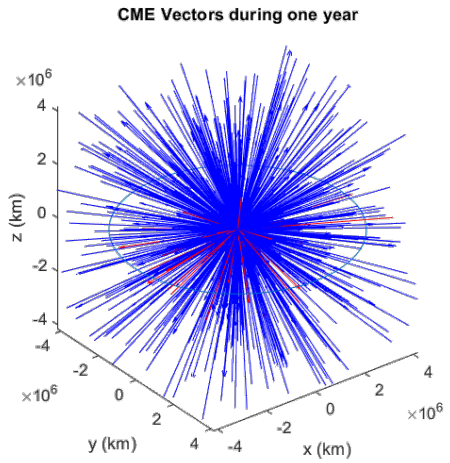

Fig. 16. *Distribution of CMEs during solar activity minima (red lines) and solar activity maxima (blue lines). A reference circular orbit is also shown.*

VI. Sail support systems.

This section discusses solar sail design and structural analysis at 1 Au and 10 solar radii. The structural analysis includes deflection, stress, strain, and buckling predictions. In this work, the structure is an assembly of 12 identical modules, creating a dodecagon with a 3038 m^2 area. The main geometric parameters are the mass and deformation of the structure. Two types of structures are designed. Structure V1 is designed for missions at lower solar pressure (1AU), and Structure V2 is designed for missions at higher solar pressure (10 Solar radii). Structure V2 is studied at 1300 °C using a composite material that can hold its stiffness at elevated temperatures. Both structure designs show very small deflection and stress under solar pressure and have a positive margin of safety against buckling.

VI.1. Design

Solar sail designs presented in most literature are focused on a cruciform 4 boom design where the deflection is not uniform in the structure. Booms undergo negligible deflection while the membrane experiences significant deflection especially at the middle of each quadrant where there is no support provided. In this work, the effort was to distribute the structural mass budget further to provide a greater support area for the membrane, which will reduce its overall deflection. This work utilizes the unit cell or modular approach to facilitate both analysis and manufacturing of the solar sail. The design underwent several iterations to achieve the minimum deflection criteria in addition to a minimum structural mass. This resulting design has 12 identical modules covering a total sail area of 3038 m^2, as shown in Fig. 17 and Fig. 18. The area of the sale is dictated by the radial length of each module, which is optimized for minimum deflection. Each module is composed of a radial truss-shaped beam designed to minimize bending and deflection under solar pressure. The modules are primarily connected to each other at 2 locations (close to the center and at the perimeter end of the sail) and in addition to 3 other locations (close to the center, mid-section, and perimeter of the sail).

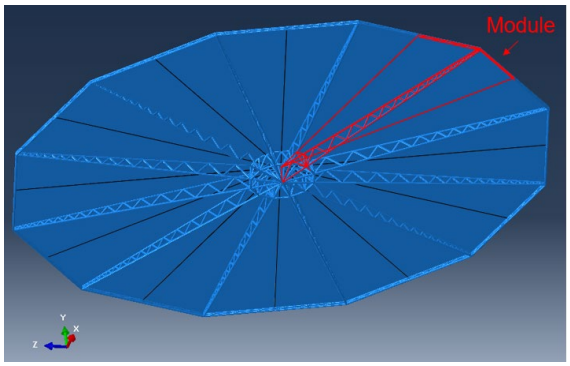

Fig. 17. *Solar Sail*

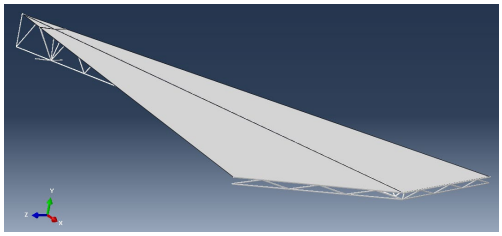

Fig. 18. *Solar sail module or unit cell*

Each solar sail module comprises the structural support, thin membrane (2.5 micrometers), and cables for connections, as shown in Fig. 19. Kevlar cables are used to both connect the membranes to the structure and to pretension the membrane to reduce membrane deflection under solar pressure. The Kevlar cable diameter and length are 0.5 mm and 5cm, respectively. The membrane material can be Kapton or SiN, depending on the mission. The cable total mass is 0.054 kg, the Kapton membrane mass is 11.94 kg, and the SiN membrane mass is 24.3 kg, given the densities listed in Table 4.

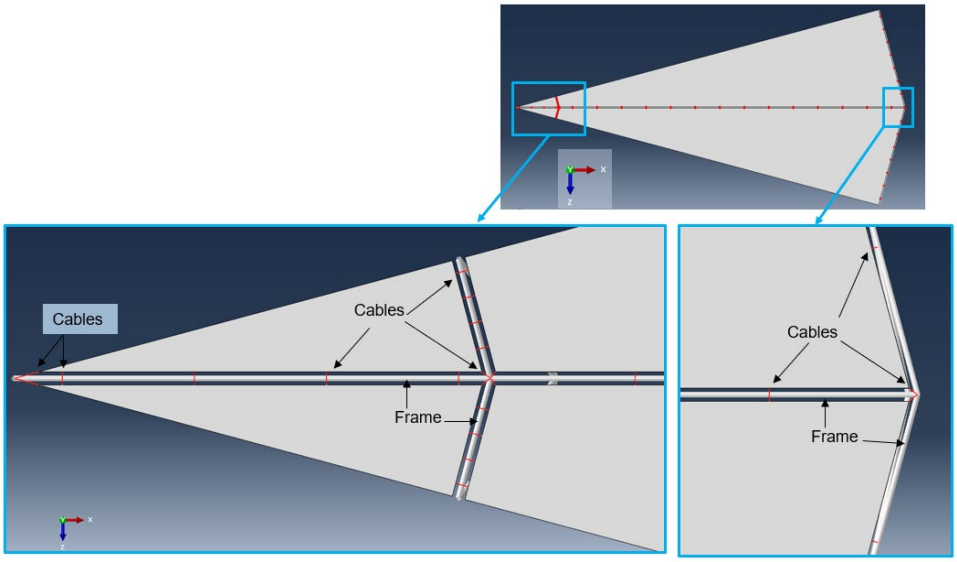

Fig. 19. *Solar sail components and connections*

VI.2. Structural Analysis

The main parameters that define the mass and stiffness of the composite structure are the length of the radial beam in each module (L), the radial beam taper (H and h), and the tube profile (r and t), as shown for the module in Fig. 20. The design iterations went through two stages. The first set of simulations was focused on finding a reasonable length and taper of the radial beam considering its effect on the mass and beam deflection when under solar pressure. After identifying the proper length and taper, the design underwent further analysis with modifications to the radius (r) and thickness (t) of the composite material tubing. A finite element model was developed for the design structure (Fig. 20), and a parametric study was performed to identify the best-performing structure having minimum mass. For a composite material structure, the results show a structure with L=31.82 m, H=2.0 m and h=0.3 m dimensions. Following this analysis, a Finite Element Analysis (FEA) was performed to find the best tube profile (r and t) that will result in minimum deflection under solar pressure at 1 AU and 10 solar radii without buckling. These studies are discussed in detail in the following sections.

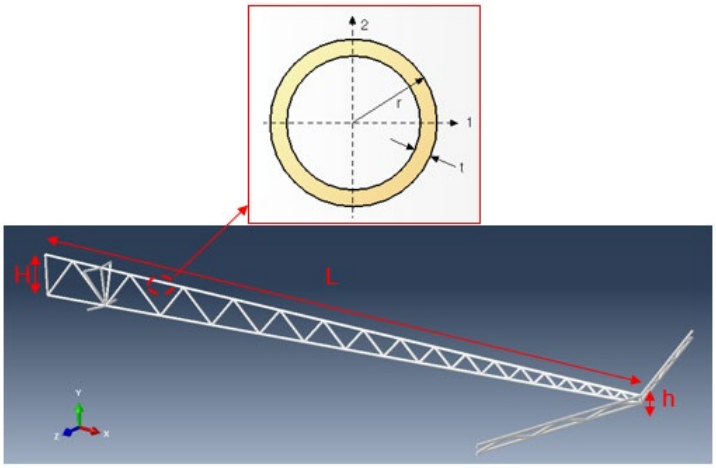

Fig. 20. *Structure V1 module*

Structure V1

Structure V1 is designed for missions at 1AU (solar pressure of 9.12 x 10^{-6} Pa) to compare with existing designs available in the literature, namely the cruciform 4 boom design reported in [10]. Optimizing the structure shown in Fig. 20 for minimum mass and deflection suggested a tube profile with 84-micron thickness and 3 mm radius for the composite structure. The dimensions and mass breakdown for Structure V1 are shown in Table 3. The material properties used in our analysis are listed in Table 4.

Table 3. *Structure dimensions and mass*

Structure	Material	t[µm]	r[mm]	Mass[kg]
V1	Composite1	84	3.0	6.47
V2	SiC-SiC composite	84	7.5	26.1

Table 4. *Material properties*

Components	**Material**	**ρ [Kg/m^3]**	**$E_{20\ ^\circ C}$ [GPa]**	**$E_{1300\ ^\circ C}$ [GPa]**	**Poisson's Ratio**	**Limit Stress $_{1300\ ^\circ C}$ [MPa]**	**Strain to failure$_{1300\ ^\circ C}$ [%]**
Structure	Composite1 [10]	2050	131	N/A	0.30	N/A	N/A
Structure	SiC-SiC Composite [11]	2796	285	250	0.24	150	0.3
Cables	Kevlar [12]	1440	62	N/A	0.36	N/A	N/A
Membrane	Kapton [10]	1572*	2.48	N/A	0.34	N/A	N/A
Membrane	SiN [13]	3200	56.2	N/A	0.3	N/A	N/A

Due to design symmetry, the Finite Element Model (FEM) is used for a single module, and the results are patterned with axial rotation to represent the overall behavior of the total structure. The FEM for the module (Fig. 20) is developed by applying symmetry boundary conditions (BCs) at the end of circumferential beams and applying solar pressure as an average line load to the structure. Also, the module is fixed from free body motions at the central axis. FEM simulations are performed in Abaqus using linear beam elements (B31). The material properties used for structure V1 (Composite1) are directly obtained from a 4-boom cruciform solar sail design from the literature [10] and are mainly used here to evaluate the deflection of the new design while keeping the same material (the type of the composite is not specified in the literature). The transverse deflection and axial stress in the tubes are computed and shown in Fig. 21 and Fig. 22 for structure V1. The transverse deflection gets to its maximum (58 µm) at the perimeter. Also, the maximum axial stress (Fig. 22) and strain (Fig. 23) in the tubes are located at the center core of the structure with values reaching 0.01 MPa and 0.1 micro-strain. Even though the strength properties are not reported for Composite1 in the literature, such a low level of stress and strain should not be a concern for this material.

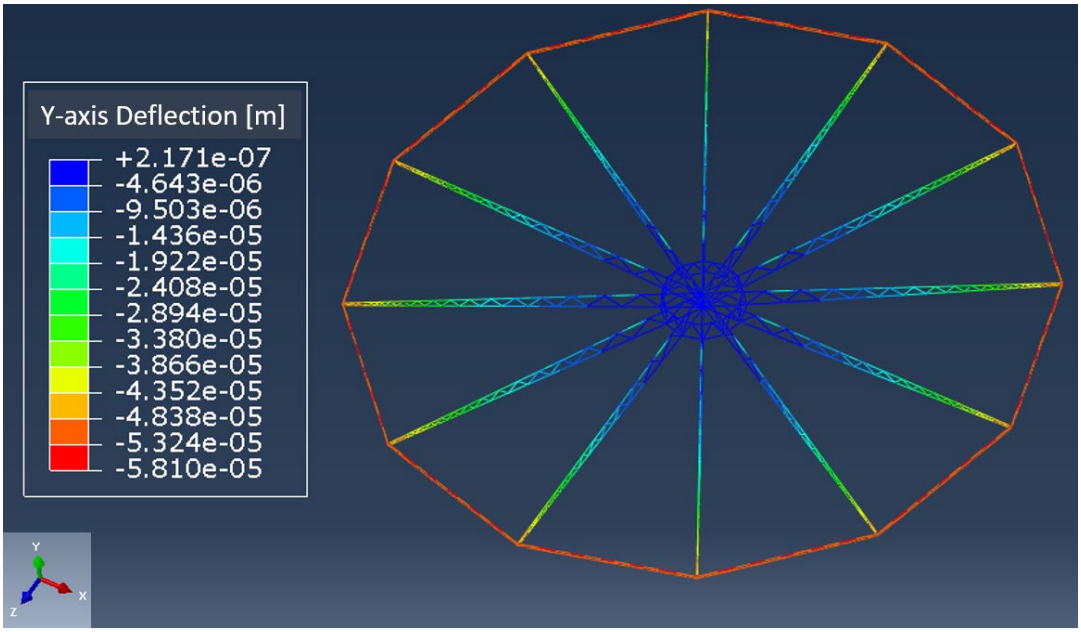

Fig. 21. *Transverse deflection in Structure V1 at 1 Au*

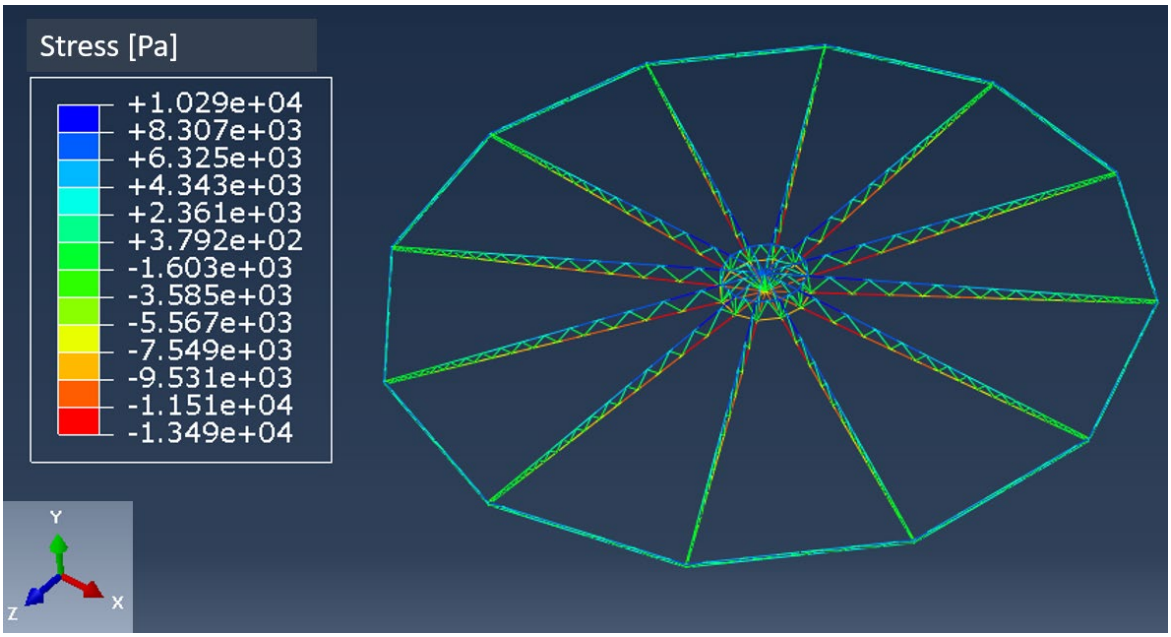

Fig. 22. *Structure V1 axial stress in tubes at 1 Au*

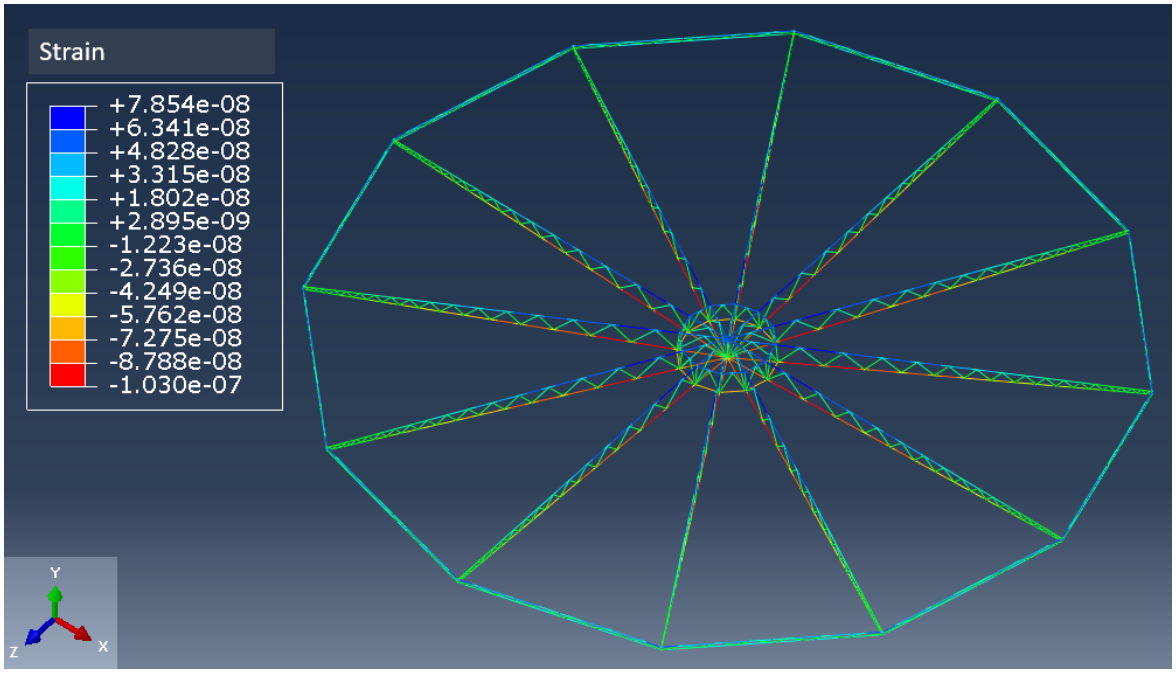

Fig. 23. *Structure V1 axial strain in tubes at 1 AU*

We also investigated the buckling of the structure to validate its stability under solar pressure at 1 AU. A buckling study is performed in Abaqus using the same loading and boundary conditions described earlier. The buckling shape for the first mode is shown in Fig. 24, with an eigenvalue of 14.9. This suggests that Structure V1 can hold up to 14.9 times the applied load before buckling.

Considering a factor of safety of 1.25, the margin of safety for buckling can be computed using the following equation.

$$MS_{Buckling} = \frac{Eigenvalue}{FS} - 1 = \frac{14.93}{1.25} - 1 = 10.9$$

Having a positive margin ($MS_{Buckling} = 10.9$) shows that the designed structure is safe against buckling under the applied load.

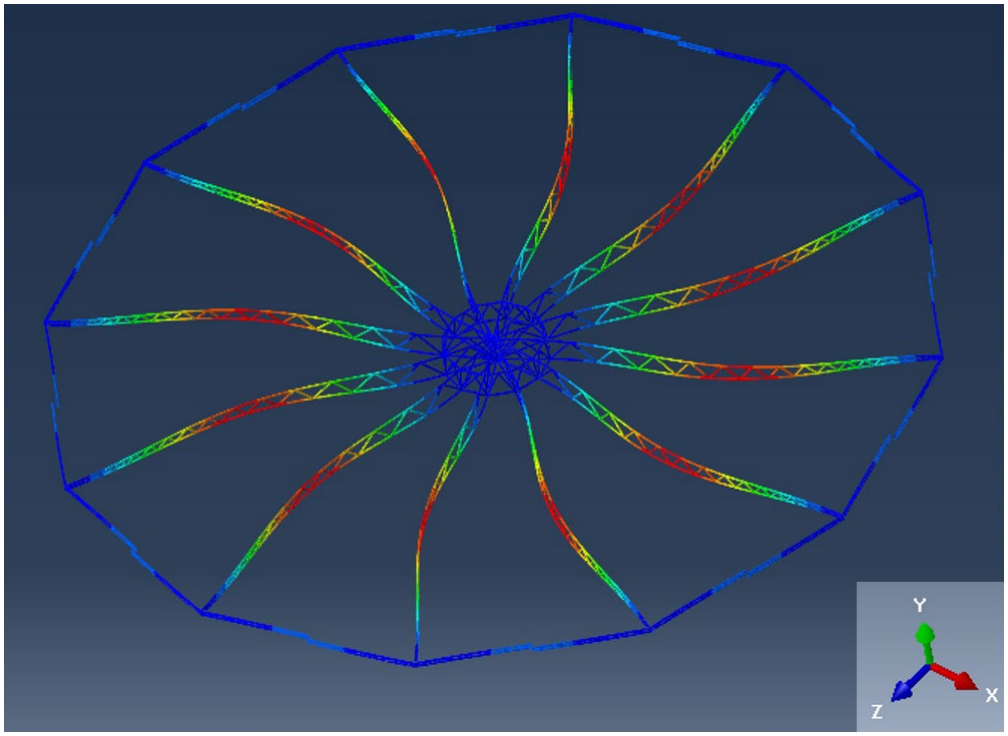

Fig. 24. *Structure V1 buckling shape (mode1, scale factor of 2)*

Structure V2

Structure V2 is designed for missions at 10 solar radii with much higher solar pressure compared to Structure V1 at 1 AU (solar pressure at 10 solar radii is about 4.2 x 10^{-3} Pa, which is 460 times larger than at 1 AU). The Structure V1 design was used as the base design for the Structure V2 effort. Structure V1 buckles at higher loads and buckling is at the center of the radial beams (red sections shown in Fig. 24). We mitigated this failure mode by adding a mid-section to reduce the free radial beam length as shown in Fig. 25 and Fig. 29. We also improved the design further by increasing the composite tube radius from 3 mm to 7.5 mm. It is important to notice that increasing the tube radius has a greater effect on the second moment of inertia and, eventually, the rigidity of the structure compared to increasing the tube thickness. This can be seen from the following equation, where the second moment of inertia (I) increases linearly with respect to tube thickness (t). However, the average radius of the tube has a cubic effect on the second moment of inertia. Both the thickness (t) and radius (r) of the tube have a linear effect on the tube mass (m), as shown in the following equation where l is the tube length and ρ is the density. Structure V2 has a mass of 26.1 kg, as tabulated in Table 3.

$$I_{thinWall} = t * \pi * \left(\frac{r_{out}+r_{in}}{2}\right)^3$$

$$m_{Tube} = 2\pi rtl\rho$$

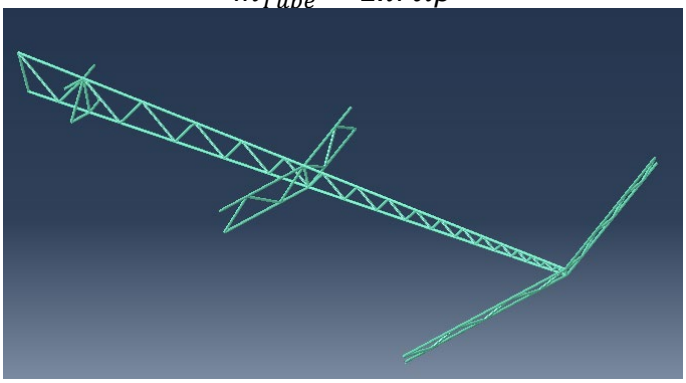

Fig. 25. *Structure V2 module*

In addition to the mid-section reinforcement and increasing the tube radius, we used Silicon Carbide/ Silicon Carbide (SiC-SiC) composite material for Structure V2, considering its high stiffness at elevated temperatures. It can be seen from Table 4 that the stiffness of this composite does not significantly drop at elevated temperatures up to 1300 °C. Since Structure V2 is aimed for missions at closer distances to the sun (10 solar radii), we considered the reduction in the stiffness at elevated temperatures in our design and used SiC-SiC material properties at 1300 °C in our simulations. The FEM for Structure V2 is developed similar to the one described in the previous section, and the deflection and axial stress in the tubing are shown in Fig. 26 and Fig. 27. It can be seen that the transverse deflection, at its maximum, is 3.7 mm and occurs at the perimeter of the structure. Also, the axial stress in the tubing reaches its maximum of 2.1 MPa around the center core of the structure. Given that SiC-SiC composites have a proportional limit stress of 150 MPa at 1300 °C, as listed in Table 4, a magnitude of 2.1 MPa is not an issue. Moreover, the axial strain in the Structure V2 tubing (Fig. 28) reaches a maximum of 8.3 micro-strain close to the center core of the structure, where our simulations showed the maximum axial stress. This strain is also much smaller than the strain-to-failure at 1300 °C for a SiC-SiC composite ($\text{SiC-SiC}_{\text{strain to failure at 1300 °C}}$ = 0.3 %, listed in Table 4).

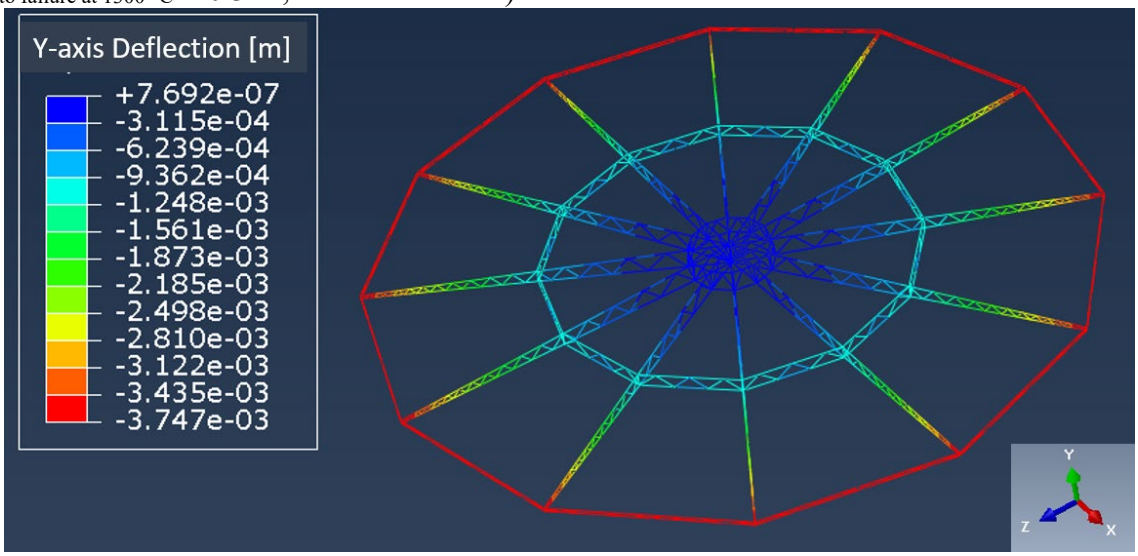

Fig. 26. *Transverse deflection in Structure V2 at 10 solar radii*

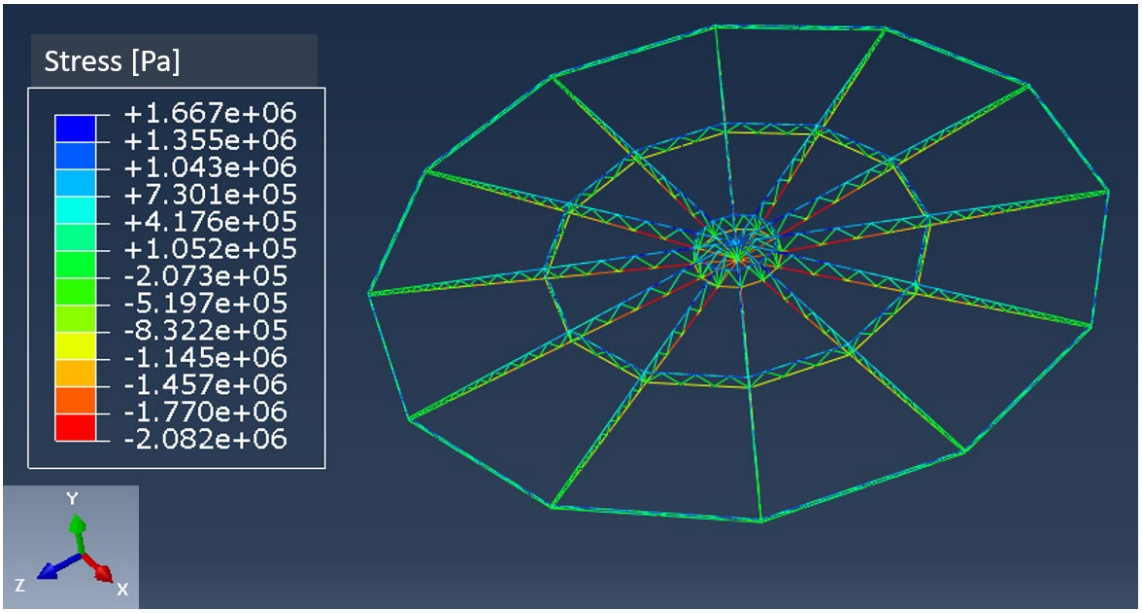

Fig. 27. *Structure V2 axial stress in tubes at 10 solar radii*

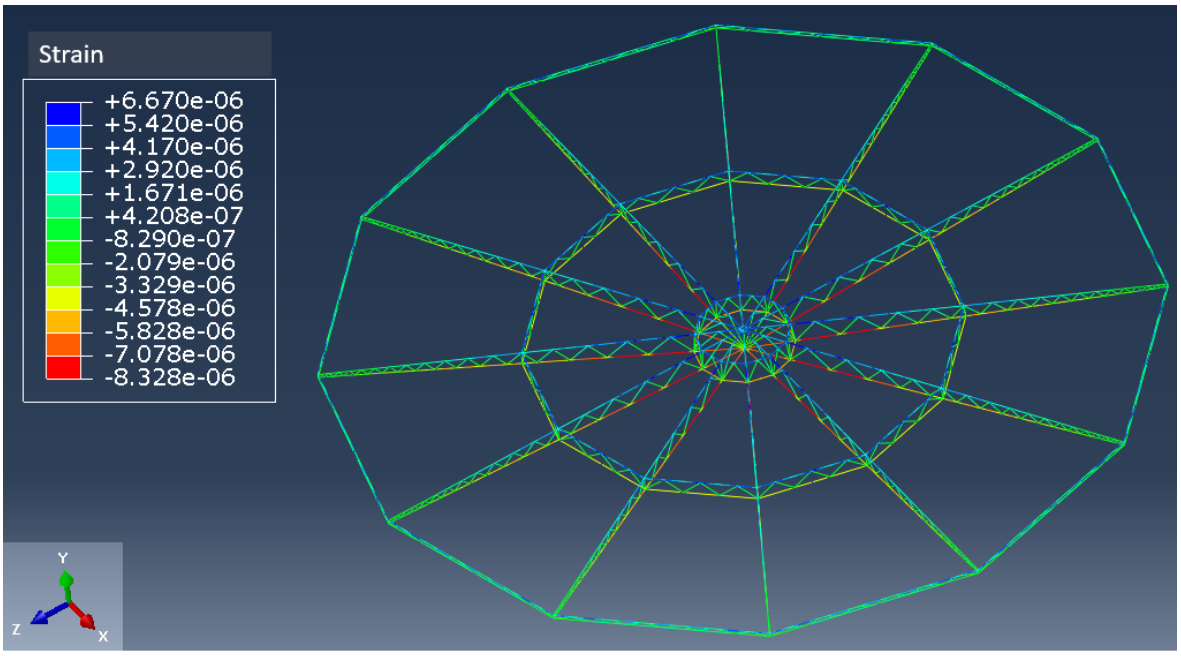

Fig. 28. *Structure V2 axial strain in tubes at 10 solar radii*

Like the previous section for Structure V1, we performed a buckling analysis for Structure V2 to investigate its stability at 10 solar radii. Fig. 29 presents the buckling shape of the first mode. The mode has an eigenvalue of 2.7, suggesting that the designed structure will be stable to buckling up to 2.7 times the applied load. Again. Considering a safety factor of 1.25, the calculated margin for buckling is 1.16 (see equation). The positive margin suggests that the design will not buckle and is safe for such loading.

$$MS_{Buckling} = \frac{Eigenvalue}{FS} - 1 = \frac{2.7}{1.25} - 1 = 1.16$$

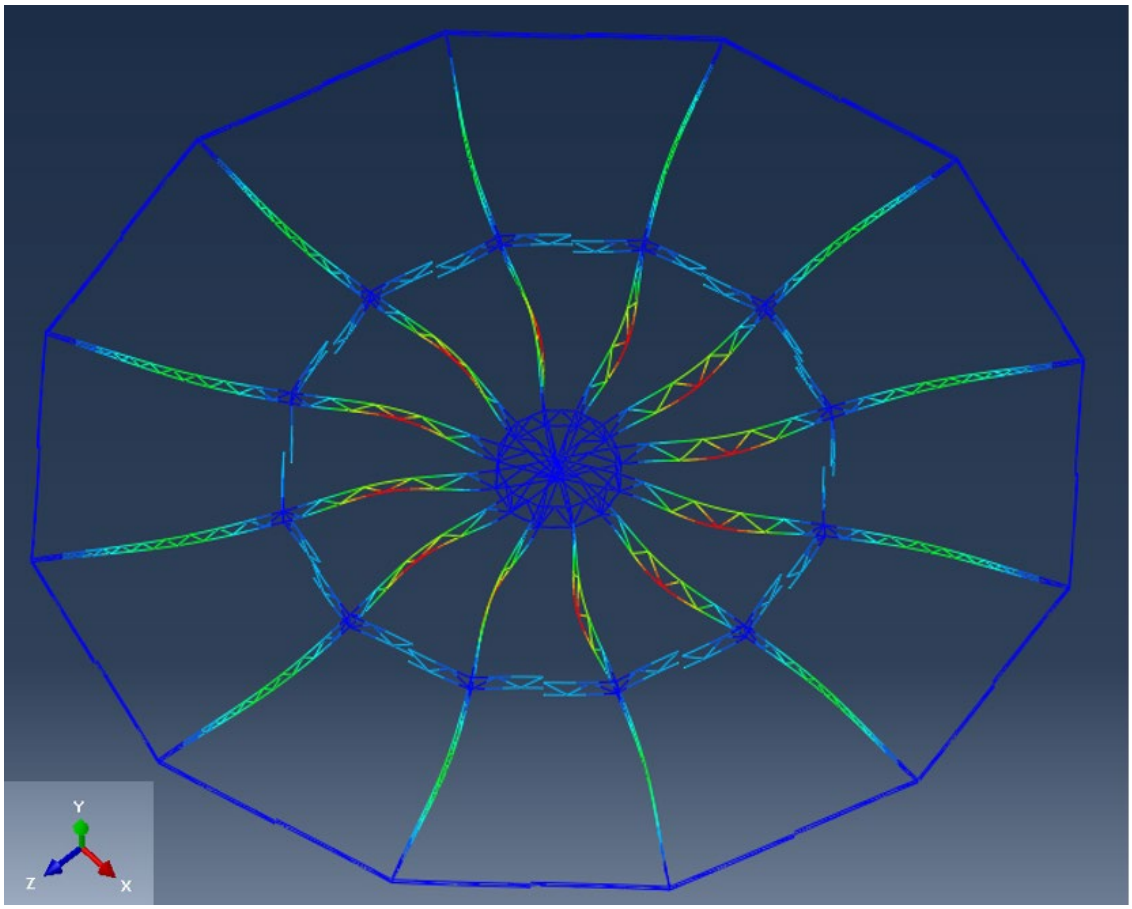

Fig. 29. *Structure V2 buckling shape (mode1, scale factor of 1)*

VI.3. Architecture Investigation Conclusion

The solar sail architecture investigations have focused on designing a solar sail support structure that has the minimum possible mass and holds a micro-thin membrane reflecting material with the goal of minimizing the overall deflection under solar radiation pressure. The successful design is a 12-sided polygon (dodecagon) made of 12 identical modules (unit cells). Each module is composed of composite material tubing with a uniform profile (radius and thickness). The unit cell module has a radial taper, as shown in Fig. 20 and Fig. 25. Here, we listed the primary outcomes of the analysis.

- The Structure V1 design is intended to compare the mass and deflection with a conventional cruciform 4 boom design found in the literature. The design shown in Taleghani et al. [10] includes 4 booms with a mass of 25.79 kg and covers a square area with a side of 70 m and resulting mass-to-area ratio of 21.2 g/m^2. Structure V1 has a total mass of 6.47 kg and covers 3038 m^{2,} resulting in a mass-to-area ratio of 2.13 g/m^2. It is also 10 times smaller than the conventional 4 boom design reported in Taleghani's article. The deflection of the sail booms in Taleghani et al. [10] is negligible like the negligible deflection values computed for Structure V1 in this work (Fig. 21). However, the conventional 4 boom design with 70 m side length reported in Taleghani et al. has larger spans of unsupported membrane compared to Structure V1 as shown in Fig. 30. This suggests that for the same membrane material, the membrane will deflect less in Structure

V1 compared to the conventional 4 boom design. Moreover, adding a mid-section, as done in Structure V2, reduces the deflection even further.

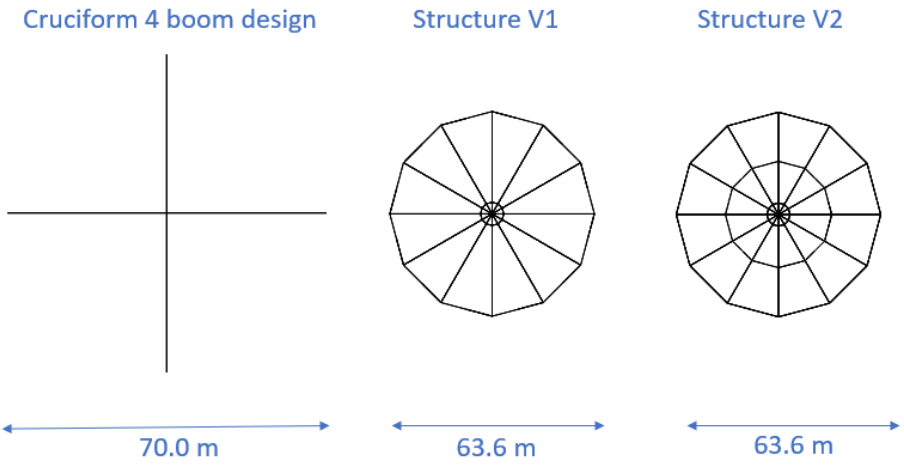

Fig. 30. *Top view of booms in Taleghani et al. "Cruciform 4 boom design" [10] and tubes in "Structure V1" and "Structure V2" produced in this work*

- Missions operating closer distance to the sun raise the concern of structural deflection and stability given the higher solar radiation pressure and elevated temperatures. The Structure V2 design is intended for missions at 10 solar radii with temperatures at 1300 °C. The design produced a 1.16 margin of safety against buckling. In addition, the axial stress and strain in the chosen SiC-SiC composite tubing were found to be not significant when compared to the material allowable. Moreover, the maximum transverse deflection on the perimeter of the structure is 3.75 mm, which is negligible given the 31.8 m radial span.
- The structures as designed could have smaller mass by reducing the tube thickness. In this analysis, the tube thickness has been kept at 84 microns in both Structure V1 and V2 to make feasible fabrication, considering that the SiC-SiC composite fiber diameter is 20 microns [11].

VII. The sailcraft design

Extreme solar sailing has a unique opportunity to pave the way to a range of breakthrough science and exploration missions. One particular interest to us is the following two mission concepts:

- **Fast Transit Interstellar Probe (FTP)**, which aims to reach 500 AU in 10 years. Our goal is to explore interstellar medium composition, its anisotropy, and its interaction with the heliosphere. The mission concept will also enable fast flyby multi-probe missions to outer planets, Kuiper belt objects, and probing of elusive Planet X (at >400 AU).
- "**Corona-Net**" (CNET) – A heliophysics science mission that aims to send a formation of sailcraft to examine solar phenomena at $< 5R_{\odot}$ at arbitrarily high inclinations, including poles.

We are not aware of any other mission concepts that set similarly audacious objectives. Yet, our study shows that these science objectives can be reached in the foreseeable future. Specifically, the Fast Interstellar Probe mission concept would enable for the first time to measure and map the heliosphere and its interaction with the interstellar medium along many directions, including out of ecliptic. The mission will also enable measuring interstellar medium composition. We further anticipate that the mission concept may be repurposed to probe high inclination and eccentricity

trans-Neptunian objects (e.g., Sedna or Planet X). A simpler mission concept might be comprised of a heavier (20-30 kg) and slower spacecraft (~30 AU/yr), which would examine outer planets/moons and Kuiper belt objects. The Corona-Net mission, in turn, will enable very high-resolution *in situ* spatio-temporal mapping of solar magnetic field and corona plasma in an extreme vicinity of the sun and at high inclinations (e.g., poles). To date, understanding the origin and the dynamics of the solar magnetic field remains one of the major unsolved problems. The mission will bring important data that would help further elaborate theoretical models.

As the two mission concepts share the utility of extreme metamaterial solar sailing, the Corona-Net mission concept also serves as a precursor mission for a Fast Transit Interstellar Probe. Indeed, from a technology development standing point, the Corona-Net mission puts less stringent requirements on spacecraft bus and solar sail design while at the same time validating key elements of extreme solar sailing: the ability to reach arbitrary inclinations and small perihelia, sail materials, high-temperature sail controls, navigation in the vicinity of the sun, ultralight sail architecture, and formation flying. Key differences between the architectures of the two mission concepts lie in sail area to spacecraft mass ratio ($A/m \geq 500 m^2/kg$ for a fast transit probe traveling at 60 AU/yr, and $\frac{A}{m} = 50 - 100\ m^2/kg$ for Corona-Net), a need for a small form factor radioisotope power source for the interstellar mission, and the miniaturization of scientific instruments.

In designing the spacecraft, we parsed the satellite into the bus, which contains all the electronics (COMM/C&DH, ADACS, power, and payload), and the primary propulsion system which is the sail and its support structure. Analysis of both the CNET and FTP missions reveals the need for low-mass materials and an integrated packaging architecture. This means a lightweight bus. To address these challenges, we relied on The Aerospace Corporation's Concept Design Center (CDC). The CDC conducts space vehicle design and mission architecture simulations based on concurrent engineering methodology (CEM). While the CDC approach requires a room full of SMEs, a mobile version of the CDC, designed for microsatellite development, was modified for a spacecraft bus design in the mass range of 10-30 kg. The modified CEM tool is an interconnected set of spreadsheets that contain Aerospace's knowledge in the design of space vehicles mixed with best practices from the industry. The tool permits trade space analysis to be done while tracking mass, power, and volume budgets along with key spacecraft operational modes (e.g., during communications, thrusting). The tool becomes especially useful when developing a concept of operations (CONOPS) for a mission, given the limits of low size, weight, and power (SWaP) spacecraft. Because the available commercial technology for CubeSats and Nanosats has vastly improved in the past decade, a trade space analysis can be done for both the CNET and FTP missions using commercial off-the-shelf (COTS) components. The major differences in the bus design between the two missions are the payload sensor and the power source. The FTP mission requires a radioisotope power source (RPS), while the CNET mission can operate on solar arrays.

Three satellite bus shapes were considered. A round disk 0.3 m dia., one that is 1.13 m dia., and a prismatic shape represented by the CubeSat class of vehicles. The round disk design has structural strength advantages and area for radiative cooling, while the prismatic shape has space heritage with the CubeSat/Nanosatellite spacecraft. Given the manufacturing technologies of today

with space structural materials, both designs can be manufactured at moderate cost. Table 5 presents the key components of the spacecraft bus as tabulated by the CEM tool.

Table 5. *Spacecraft bus subsystem and components.*

Spacecraft subsystem	**Key COTS components**
Attitude Determination and Control System (ADCS)	• 4X Blue Canyon RWP50 reaction wheels (58 mm x 58 mm) • 1X BCT Nanotracker • 1X STIM210 Inertial measurement unit • 4X Course sun sensors (Pointing knowledge 18 arcsec)
Command Data and Handling (CDH)	• CubeSat CDH, data storage 204.8 GB
Communications (COMM)	• Iris Radio with high-gain reflect array (8kbits/s from 1.05 AU) – similar to the NASA MarCO mission
Electrical Power System (EPS)	• RPS for Fast Transit Mission: 25 We Brayton generator, ½ scale of commercial unit • Solar power for Corona-NET Mission: body-mounted solar cell arrays – based on solar flux of 5468 W/m2 solar flux. • GOMSpace BPX 2s-4p battery (82 W-hr., 10.4 A-hr., 0.5 kg, 86 mm x 80 mm)
Secondary propulsion for precision attitude control	• 3X Morpheus MultiFEEP thruster modules (50 mm x 50 mm)

Table 6 presents the common best estimate (CBE) mass budget for the three spacecraft shapes and for the two missions as identified by the mission power source. The mass budget is broken down into subsystems. There is no mass contingency added to the values shown, but the industry practice is to add up to 25%. We note that in this first-order analysis, the bus mass varies between 7-12 kg, suggesting that the requirement for the CNET mission solar sail area might be moderate. A second observation is that the total bus mass for a solar-powered vehicle is smaller than that for an RPS-carrying mission. RPS units are massive, and they require bespoke radiative cooling needs. A third observation is that there are but a few kg differences in the CBE mass budget for the different spacecraft bus shapes. The CEM tool catalogs the mass density (kg/m^3) as a spacecraft design parameter, this parameter reflects the extent to which systems must be integrated in packaging. When compared to industry standards, the mass density is a harbinger of the packaging-integration cost required to manufacture the space vehicle. For high-density electronics, the iPhone 12 Pro has a mass density of □2435 kg/m^3. A traditional satellite bus has a much lower mass density (e.g., GPS Block IIR at launch 144 kg/m^3) because it is designed to mount the subsystems on a scaffold. CubeSats/NanoSats require more efficient packaging. NASA's MarCO, a 6U CubeSat, has a mass density of 2250 kg/m^3. For the data presented in Table 4, a 6U CubeSat would have a mass density of 1167 – 1667 kg/m^3, while the mass density for the 1.13 m dia. shape bus would be 5 times lower.

Table 6. *Bus mass budgets for three bus shapes and for the CNET and FTP missions. †RPS is a scaled down 25We Brayton generator.‡ Body-mounted solar arrays have a 90% packing factor for the prismatic design and ~ 50% packing factor for round shapes.*

Space Craft Design	Round 0.3 m Dia.		Round 1.13 m Dia.		Prismatic CubeSat Design	
Mission Power Source	RPS	Solar Powered	RPS	Solar Powered	RPS†	Solar Powered‡
Bus Total (CBE mass kg)>>	10.0	6.6	12.2	8.6	10.7	7.0
Attitude Determination and Control	1.4	1.4	1.4	1.4	1.4	1.4
Command and Data Handling	0.8	0.8	0.8	0.8	0.8	0.8
Communications/TT&C	2.2	2.2	2.2	2.2	2.2	2.2
Electrical Power	4.0	0.7	4.0	0.6	4.0	0.6
Harness	0.1	0.0	0.1	0.0	0.1	0.0
Propulsion	0.9	0.9	0.9	0.9	0.9	0.9
Structure/Mechanisms	0.2	0.2	2.3	2.3	0.9	0.7
Thermal Control	0.4	0.4	0.5	0.4	0.4	0.4

Table 7 presents the CBE power budget in three key operational modes: during charging, RF communications, and during thrusting. The power budget is also shown for the three spacecraft shapes. Each analysis is for a solar array power source. The analysis for the RPS concepts as a function of spacecraft shape did not show much change, so we report the nominal power budget for the three key operational modes. There are also no power contingencies added to these values. Typically, a 10-15% contingency is added to the CBE values. The first observation from Table 7 is that the largest power consumption is during communications (35We for Communications TT&C), followed by thrust operations. We have assumed that, in most cases, communications and thrusting would not be done simultaneously to save on battery mass. A second observation is that there is power consumed during charging operational modes, this is the spacecraft maintaining internal services while charging batteries. It also applies to the case of the bus that carries the RPS which is continually charging because of the continual radioisotope decay. In the case of a CNET mission and for a solar array electrical power source, maintaining high power charging should be faster in comparison to charging in Earth orbit (e.g., 100 times more flux at 0.1 AU – 21.5 solar radii). This would also mean that a 1m size bus, as compared to a CubeSat class bus (e.g., 6U) would have more power available for the mission.

Table 7. *Bus power budget for three spacecraft operational modes. Also, for three bus designs given a solar power source and for an RPS dependent bus. Power budget analysis is essentially the same for all RPS concepts.*

Satellite Subsystems	Power Mode 1: **Charging**				Power Mode 2: **RF Comm**				Power Mode 3: **Thrusting**			
	Solar Power 0.3m dia. Bus	Solar Power 1.13 m dia. Bus	Solar Power CubeSat class Bus	RPS Dependent Bus	Solar Power 0.3m dia. Bus	Solar Power 1.13 m dia. Bus	Solar Power CubeSat class Bus	RPS Dependent Bus	Solar Power 0.3m dia. Bus	Solar Power 1.13 m dia. Bus	Solar Power CubeSat class Bus	RPS Dependent Bus
Bus Total (CBE Power, W)>>	**9.9**	**17.2**	**10.0**	**7.8**	**44.9**	**52.2**	**45.0**	**42.8**	**28.9**	**36.2**	**29.0**	**26.8**
Attitude Determination and Control	3.3	3.3	3.3	3.3	3.3	3.3	3.3	3.3	3.3	3.3	3.3	3.3
Command and Data Handling	3.1	3.1	3.1	3.1	3.1	3.1	3.1	3.1	3.1	3.1	3.1	3.1
Communications-TT&C	0.0	0.0	0.0	0.0	35.0	35.0	35.0	35.0	0.0	0.0	0.0	0.0
Electrical Power	2.8	10.0	2.9	0.3	2.8	10.0	2.9	0.3	2.8	10.0	2.9	0.3
Propulsion	0.0	0.0	0.0	0.0	0.0	0.0	0.0	0.0	19.0	19.0	19.0	19.0
Thermal Control	0.7	0.8	0.7	1.1	0.7	0.8	0.7	1.1	0.7	0.8	0.7	1.1

To provide more capability to CubeSat/Nanosatellite missions, The Aerospace Corporation has been investigating the utility of a spacecraft form called a DiskSat [4]. Like its namesake, DiskSat is a 1 m dia. flat “pancake” structure, 2.5 cm thick, and can accommodate the volume of a 20U CubeSat. The primary advantage of the DiskSat form factor is that it offers high power and a large sensor aperture compared to CubeSats. NASA has approved a demonstration flight in 2024 for the circular DiskSat [5]. We have used the available data on the DiskSat to explore its utility for the CNET and FTP missions. Table 8 provides the components that comprise the DiskSat bus for the CNET and FTP missions. Much of the subsystem components are the same between the two missions, except for the payloads and the communication approach. The CNET spacecraft bus communicates via RF X-band, while the FTP mission uses an Aerospace-developed laser communications package [6]. The DiskSat attitude control system requires 4 MultiFeep thrusters instead of 3 (Table 5).

Table 8. *Subsystem components for a DiskSat-based spacecraft bus for the CNET and FTP missions. In both cases, a nominal solar sail as the primary propulsion system has been added.*

Corona-Net Space Craft Bus	Fast Transit Probe Space Craft Bus
Solar Sail	**Solar Sail**
Design sail area: vehicle mass ratio: 100 m^2/kg Nominal sail mass set aside (kg): 5.5 kg	Design sail area: vehicle mass ratio: 200 m^2/kg Nominal sail mass set aside (kg): 5.5 kg
Payloads	**Payloads**
ECP-Lite charged particle sensor 2x NewSpace Systems NMRM-Bn25o485 magnetometers	Dragonfly Aerospace Mantis hyperspectral camera Ion, Neutral Mass Spectrometer -Dellingr[‡] Cubesat mission
ADCS	**ADCS**
4x Space Inventor REWL-30 reaction wheels 1x Hyperion Sun Sensor 2x Hyperion Technologies ST200 star trackers 1x STIM202 IMU	4x Space Inventor REWL-30 reaction wheels 1x Hyperion Sun Sensor 2x Hyperion Technologies ST200 star trackers 1x STIM202 IMU
CDH	**CDH**
AeroCube avionics: cam., SDR, AC, FGA, and EPS boards	AeroCube avionics: camera, SDR, AC, FGA, and EPS boards
COMM	**COMM**
Tendeg KaTENna 1m antenna (downlink) X-band AntDevCo patch antenna (crosslink)	Aerocube laser Comm: primary, secondary mirrors, EPS-H board
EPS	**EPS**
Body-mounted solar arrays 11s2p 18650 battery assembly (32.8 A-hr)	1x 55W Brayton radioisotope power system
Secondary Propulsion	**Secondary Propulsion**
4x Morpheus MultiFEEP thrusters, 2 operational at a time	4x Morpheus MultiFEEP thrusters: 2 operational at a time
Bus structure design	**Bus structure design**
1m diameter DiskSat sandwich, 3 kg/m^2 aerial density	1m diameter DiskSat sandwich, 3 kg/m^2 aerial density
Thermal	**Thermal**
Parametrically sized based on historical values	Parametrically sized based on historical values

Table 9 presents the mass and power budgets for a DiskSat-based spacecraft bus. The results are for both the CNET and FTP missions. The "Max expected power" is not cumulative, just the maximum power anticipated to operate key subsystems. As the primary payload, the CNET mission carries a charged particle sensor and magnetometers, while the FTP bus has a hyperspectral camera and a mass spectrometer. A notional solar sail is also added under the "payload" column. The analysis set aside 4.5 kg mass for the CNET mission and 5.5 kg for the FTP. These are notional masses and strongly depend on the materials used for the sail and support structure. The mass difference is to underscore that the FTP mission will likely require a larger solar sail area than the CNET mission. Finally, because the Aerospace DiskSat project is maturing and readying for launch, we are more confident about the systems reserve contingencies needed.

Consequently, there is reserve contingency placed on both the mass and power for both missions. The results in Table 9 show that with a DiskSat bus, by subtracting contingencies from the total CBE spacecraft bus mass, sail and payload mass can be in the range of 12-16 kg, roughly a 20-30% increase over the analysis done for the antecedent design.

Table 9. *Mass and power budgets for a DiskSat-based spacecraft bus. Max expected power is not cumulative, just the maximum power expected for operating key subsystems. ‡ A systems reserve contingency has been added to this design. † The mass of a notional solar sail propulsion system has also been added to this design.*

Corona-Net (Mass & Power)	Mass Total (kg)	Max Expected Subsystem Power (W)
Spacecraft Total	**22.6**	
Payload Total	**7.6**	
Solar Sail†	4.5	
Charged Particle Sensor	2.9	2.1
Magnetometers (x2)	0.2	0.9
Bus Total	**15.0**	
Attitude Determination and Control	0.4	2.8
Command and Data Handling	0.3	1.0
Communications/TT&C	2.5	0.0
Electrical Power	3.5	
Harness	0.3	
Propulsion	2.2	38.0
Structure/Mechanisms	2.4	
Thermal Control	0.4	3.8
Systems Reserve Contingency‡	3.0	11.4

Fast Transit Probe (Mass & Power)	Mass Total (kg)	Max Expected Subsystem Power (W)
Spacecraft Total	**27.5**	
Payload Total	**6.6**	
Solar Sail†	5.5	
Hyperspectral Camera	0.5	2.6
Mass Spectrometer	0.6	1.8
Bus Total	**20.9**	
Attitude Determination and Control	0.4	2.8
Command and Data Handling	0.3	1.0
Communications/TT&C	3.1	15.0
Electrical Power	6.9	
Harness	0.6	
Propulsion	2.2	38.0
Structure/Mechanisms	2.4	
Thermal Control	0.8	4.6
Systems Reserve Contingency‡	4.2	15.6

One major aspect of the DiskSAT bus design is the change in communication technology from RF to optical (i.e., laser). Laser communications are likely to be more important for the FTP missions, possibly traveling to the outer planets and interstellar space. To maintain a reasonable communication bit rate, an RF communication system requires a large transmit antenna. NASA's New Horizons spacecraft (Jupiter, Pluto, Arrokoth flybys) bus carried a 2.1 m diameter radio antenna. To make a solar sailcraft operate at 100 AU or farther with RF communications, the sail structure (not functional as a propulsion system after Jupiter orbit) will have to be re-shaped to act as an RF transmit antenna. Another approach is to use laser communications. Laser technology has matured such that reliability testing (ISO/FDIS 17526) now estimates over 11 years for a high-power (50W, 808 nm) laser diode pump [7]. Over that duration, an FTP spacecraft traveling at 20 AU/yr velocities would reach 220 AU (110 AU if traveling at 10AU/yr). Table 10 presents the results from a laser communication simulation tool for ranges 1 AU (CNET mission) and 200 AU (FTP mission). The laser source is a 10W near IR laser (10 cm Tx telescope). The receiving telescope has a 3m aperture. The results show that the information rate (16_PPM encoding) at 840 kbps can be transferred (link margin of 3.2 dB) from 1 AU (CNET mission) and 4 bps (link margin 3.2 dB) from a range of 200 AU. At 50 AU (Pluto + 10 AU), a communication rate of 280 bps (link margin 3 dB) can be maintained.

Table 10. *Optical communication link from a simulation tool that includes slant range atmospheric losses.*

Communication: Range= 1 AU						**Communication Range=200 AU**			
		Value	Unit	Value	Unit	Value	Unit	Value	Unit
Satellite optical transmitter	**Tx Optical Power**	10.0	W	40.00	dBm	10.0	W	40.00	dBm
	Telescope Diameter	10.0	cm			10.0	cm		
	Transmit EIRP	1.24E+13	W_i	130.92	dBWi	1.49E+11	W_i	111.72	dBWi
Channel with atmospheric loss	**Slant Range**	1.496E+08	km	1.0	AU	2.992E+10	km	200.0	AU
	Net Path Loss			366.70	dB			407.70	dB
	Received Optical Power	1.06E-14	mW	-139.73	dBm	1.06E-14	mW	-139.73	dBm
Satellite optical receiver	**Rx Telescope Diameter**	300	cm			300	cm		
	Received Optical Power	4.25E-10	mW	-93.71	dBm	1.06E-14	mW	-139.73	dBm
COMM link	**Information Rate**	840.000	Kbps			0.004	Kbps		
	Link Margin			3.2	dB			3.2	dB

While laser communication provides an advantage to the FTP mission, RF communication has an advantage for a CNET mission in which there could be multiple spacecraft flying in formation. An RF-based steerable phase array radar could be used to maintain range distance between spacecraft. The phased array radar generates known state and pose vectors for each CNET spacecraft. Fig. 31 shows a schematic of a four-spacecraft cluster. In this concept, RF power and electronics are used for both communication to Earth and for maintaining range distance. A formation flying mission enables time-synchronous data to be acquired over a large area. This enables solar scientists to tease out the extent (i.e., area) of small solar atmospheric effects. The size of the area that can be covered depends on the radar transmit power, the gain, and the radar cross section which is related to the sail area. Table 11 presents the calculated results of the maximum range to target (km) while maintaining a signal-to-noise (SNR) > 10. The results show that for a 1- or 5-watt radar transmitter and gain values of 30 dB or 20 dB, it is possible to have a satellite-to-satellite separation approaching 9 km. For a 10W transmitter and 30 dB gain, the calculations suggest a 15 km separation. Using a diamond-shaped flying formation and 15 km separation, one can imagine a lead-to-tail spacecraft distance of 26 km, which would be the range distance of the time-synchronous data.

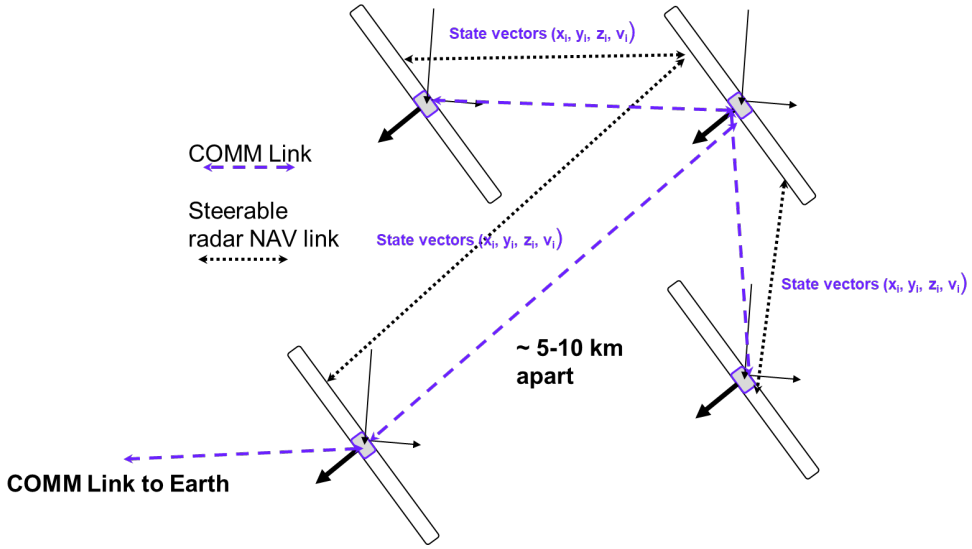

Fig. 31. *A schematic of a four-spacecraft cluster flying in formation. There is an RF communication link to Earth and an independent RF steerable radar for maintaining precision during the flight. Depending on the radar power on board range can exceed 10 km.*

Table 11. *Radar cross-section analysis as a function transmits power, gain to ensure detection with SNR > 10.*

Radar Transmit Power (W)	Gain (dB)	Sail radius (m)	Radar Cross Section of sail area (m2)	% of area used as Radar cross section	Max Range to Target (km) for SNR > 10
1	30	26	2123	30	**8.5**
5	20	26	2123	30	**4.2**
5	30	10	314	30	**8.2**
10	20	10	314	30	**3.1**
10	20	26	2123	30	**5**
10	30	26	2123	30	**15**
20	20	10	314	30	**3.5**
20	10	26	2123	30	**1.9**

VII.1. Bus protection.

As the solar sail might heat to ~>1500 K (temperature depends on the material used and perihelion distance), a dedicated shielding of the spacecraft bus to protect from the sail's thermal radiation is needed. In addition, some sail designs are partially transparent (e.g., SiN sails transmit ~20-25% of sunlight). For this purpose, we have considered a thermal shield design (Fig. 32). The shield has an architecture similar to that of a James Webb Space Telescope sunshield. Here, a multilayer blanket (which can, in fact, be comprised of high-temperature TiN sail material) is utilized to shield the thermal radiation. Our modeling shows that a 6-layer multilayer blanket with an area of a few m^2 (assuming 0.04 emissivity of the blanket layers) is capable of keeping the spacecraft bus at room temperature. We further note that heat shield design (i.e., shape and area) may be chosen to protect the spacecraft bus when the sail is at an angle to the sunline. Our estimates show that the mass of the heat shield is ~100g.

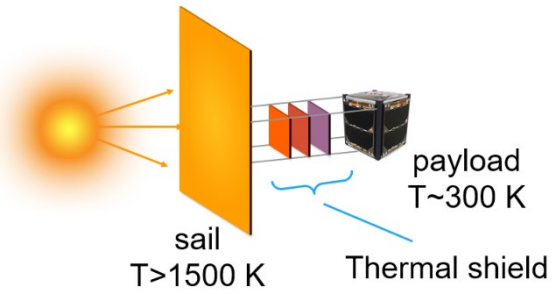

Fig. 32. *Schematic illustration of the heat shield for payload protection studied.*

VII.2. Sail Controls.

To understand sail control challenges we have developed a 2D control model assuming a square sail as a baseline design. In particular, we assume that a sail can rotate about one axis only (e.g., x-axis, as shown in Fig. 33). In our model we find the I_{xx} component of the inertia tensor about the center of mass of the entire sailcraft. We then write a 1D equation of motion:

$$\ddot{\theta} = \frac{1}{I_{xx}}\tau_c,$$

here θ denotes a sail orientation with respect to sunline, τ_c is the control torque applied.

Based on this model we have made a preliminary assessment of several approaches to controlling solar sail attitude, including active translation mass (ATM) systems (used in Solar Cruiser), variable reflectivity devices, reflectivity control devices (RCD), (used on IKAROS and Solar Cruiser), and adjustable reflective flaps (used in Sunjammer).

The forces in this case are given as:

$$\tau_{flap} = \tau_{RCD} = \frac{2}{c} S_{1AU} \left(\frac{1AU}{d_0}\right)^2 A_{eff} a \cos\theta$$

$$\tau_{AMT} = \frac{2}{c} S_{1AU} \left(\frac{1AU}{d_0}\right)^2 h_y a \cos\theta$$

where A_{eff} – effective area of a control surface for a reflective system (i.e., flaps and RCDs), a is an effective distance to the control surface from the sail center (we expect control elements to be placed at the edges of the sail), h_y is a distance over which mass is translated in case of ATM. In this model we assume that reflectivity of control surfaces can vary by 100%.

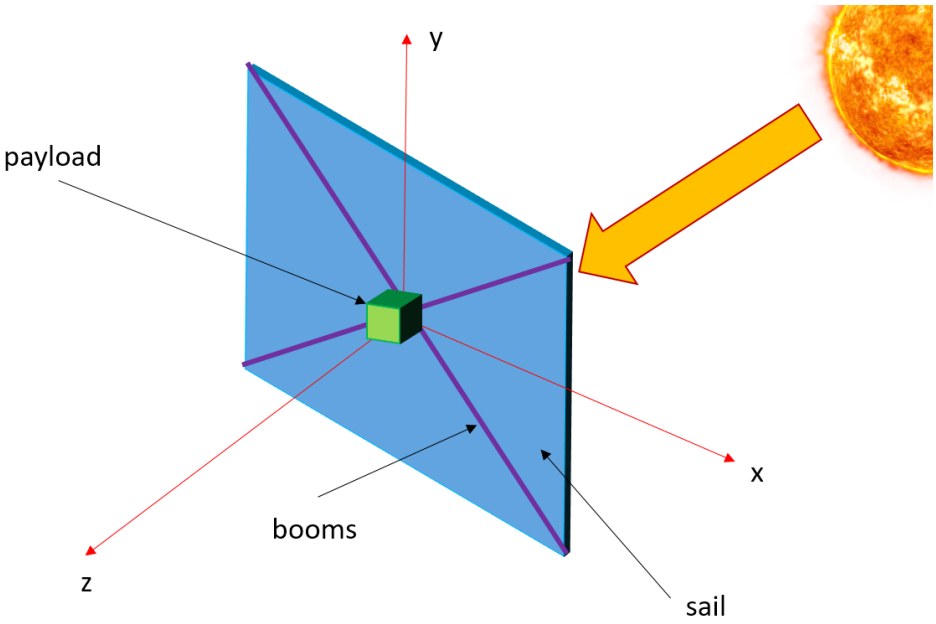

Fig. 33. *2D sail control model.*

For all of the approaches we find that in the vicinity of the sun strong radiation pressure forces induce large torques, especially for large area sails (e.g., 1 $N \cdot m$ for ~10,000 m^2 which corresponds to ~1 deg/s turn rate). This analysis suggests that the sail may be quickly reoriented (e.g., ~90 deg in just ~100 s at 5 R☼) to follow a desired trajectory. Furthermore, we note that attitude control happens at a much shorter time scale as compared to sail orbital maneuvering (i.e., ~100s to reorient the sail, whereas it takes ~1day to perform perihelion pass). Such responsivity of control system implies that the sail trajectory may be quickly adjusted during a critical pass. At the same time, large torques suggest that during a close perihelion pass the sail is very susceptible to minute perturbations in the radiation pressure. As communications with Earth will take ~16 min (both ways) and sail can be "capsized" in just 100s, a fully autonomous control system, potentially with the use of passive self-stabilizing elements is needed. In this regard perihelion pass may be conceptually compared to spacecraft re-entry.

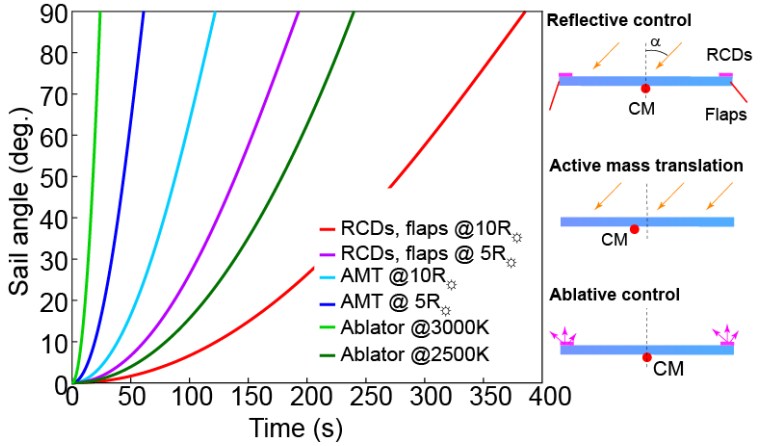

Fig. 34. *Calculated sail angle with respect to sunline for different control approaches studied.*

Due to hugh torques for large area sails, careful design of actuation and control approaches is needed. Small disturbances can also cause signifjcant influence on overall sail attitude dynamics. As such, as the spacecfrat design progresses, a more detailed study of controls and parameter safe sets is needed. Additoinally lasrge area sails would require design of novel actuators that are light-weight can be scaled to large area surfaces and exhibit fats response time. Such actuators would need to be based on controlling radiation pressure (on par with the RCDs) as these can de easily scaled to large area surfaces. Study of such actuators is an active topic and it is expected that in the near future new types of devices can be created. Furthremore, actuator for extreme solar sail missions should be capable of withstanding high fluxes of solar radiation at close perihelion approaches.

VIII. Summary of the NIAC Phase II study

• Trade studies indicate that a solar sail spacecraft capable of reaching <5R☼ and 60AU/year can be built   ○ Sail materials identified as a key technical challenge
• Two types of materials have been designed: TiN and SiN based solar sails.
• Study of the solar environment – sail materials interaction indicates that while the environment is challenging, it can be survived owing to a short duration of the perihelion pass

• Concept of operation of solar sailing is refined:
  ○ Sail controls are shown to be very responsive (~1 deg/s) near perihelion, allowing fine control over navigation and maneuvering during critical phases of the mission
  ○ Sails are used as space tugs to deliver goods to desired orbits
  ○ Smaller (10-20 kg) sailcraft perform distributed mission science objectives and/or are aggregated into a larger spacecraft

• Two mission concepts (Fast Transit Interstellar Probe and a precursor Corona Net mission concepts) are considered. Preliminary spacecraft architecture is studied
  ○ We show that a fully functional spacecraft bus with ~10kg can be created with today's technology
  ○ An approach to keeping formation flying for Corona Net mission is discussed

We have also identified areas where further technology development is needed (excluding materials development that we have discussed earlier):

- Lightweight sail support systems that can enable large sails
- Sail support systems (booms, etc.) that can handle high temperatures during close perihelion passes.
- Navigation and control near perihelion pass (likely a large degree of autonomy is needed during perihelion maneuvering)
- Control surfaces capable of operating at high temperatures
- Optical communications for interstellar missions (>200 AU, beyond the reach of Deep Space Network)
- Power systems for interstellar probe missions

- Deep space assembly (in case larger “flagship” class missions are required)

IX. Roadmap

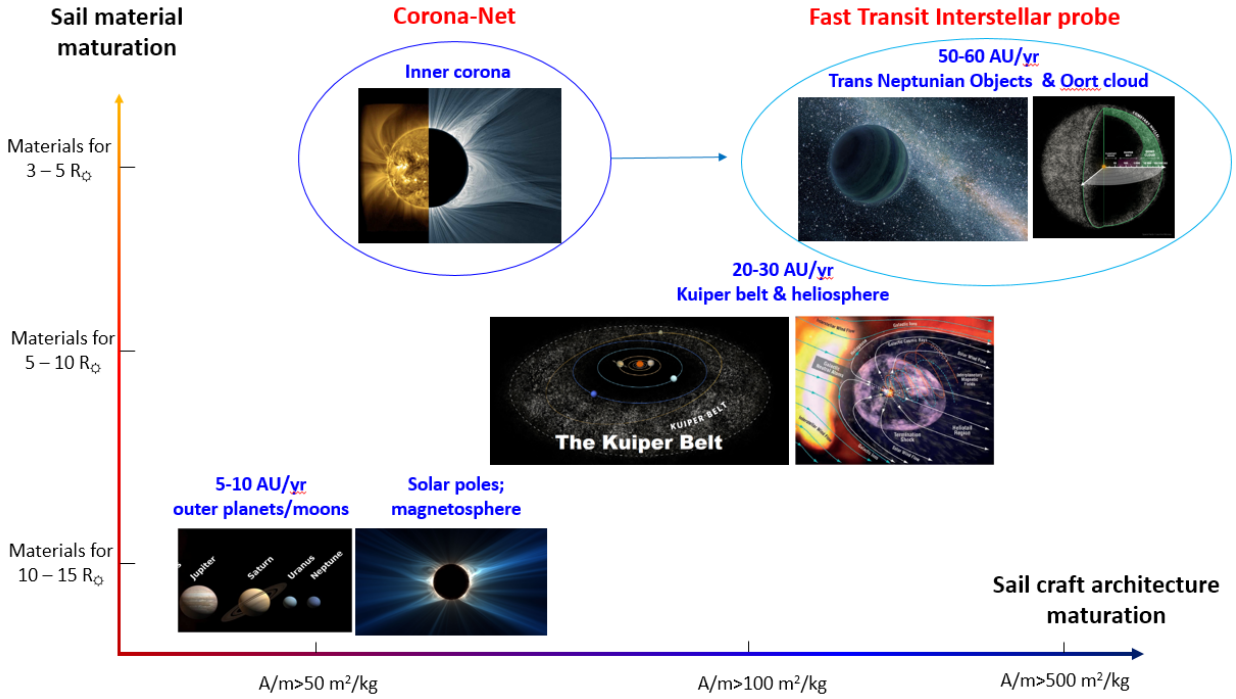

Fig. 33. Science roadmap. *With the development of sail materials for close solar approaches and the development of lightweight and large-area sail systems, novel breakthrough missions would be enabled. In the near term, we foresee fast interplanetary and solar imaging missions. With further advancement of solar sailing technology exploration of Kuiper belt and outer heliosphere would become regular. With materials that can bring sails to <10R☼ , breakthrough exploration missions of the sun become possible. Such exploration is the goal of our Corona Net mission concept. Corona Net also serves as a precursor mission for a Fast Transit Interstellar Probe (i.e., enables mature critical technologies for future interstellar flight). Ultimately, with sail materials that can reach 3-5R☼ and lightweight sailcraft architectures (>500 m^2/kg) exploration of deep interstellar space (>200AU – 1000AU) becomes regular. Such missions will advance the science of outer solar system celestial bodies, bring new data about the composition of interstellar plasma, and allow testing of fundamental physics at the borders of our solar system.*

References:

1. E. Stone “The Voyagers” Nature Astronomy 1, 896 (2017).
2. M. Macdonald, G. W. Hughes, C. R. McInnes, A. Lyngvi, P. Falkner and A. Atzei, “Solar Polar Orbiter: A Solar Sail Technology Reference Study,” J. Spacecraft and Rockets 43, 906 (2006).
3. G.L. Matloff and E.F. Mallove, “Solar Sail Starships—The Clipper Ships of the Galaxy”, JBIS, 34, 371-380 (1981).
4. G.L. Matloff and E. F. Mallove, “The Interstellar Solar Sail: Optimization and Further Analysis”, JBIS, 36, pp.201-209, 1983
5. C. Sauer “Solar sail trajectories for solar-polar and interstellar probe missions,” AAS/AIAA Astrodynamics Specialist Conference 99-1367 (Girdwood, Alaska, 1999)
6. D. Spieth and R. Zubrin, “Ultra-Thin Solar Sails for Interstellar Travel” NIAC Phase I Final Report (1999)
7. P.C. Liewer et al., “Interstellar probe using a solar sail: Conceptual design and technological challenges,” in The Outer Heliosphere: The Next Frontiers, Edited by K. Scherer, Horst Fichtner, Hans Jörg Fahr, and Eckart Marsch COSPAR Colloquiua Series (Amsterdam: Pergamon Press, p.411, 2001)
8. C. McInnes, “Solar Sailing: Technology, Dynamics and Mission Applications”, Springer-Praxis, Chichester, UK, 2005.
9. G.L. Matloff, “Deep-Space Probes”, 2nd ed., Springer-Praxis, Chichester, UK (2005)
10. G.L. Matloff, “The Beryllium Hollow Body Sail and Interstellar Travel”, JBIS, 59, pp.349-354, 2006.
11. L. Johnson, R.M. Young, E.E. Montgomery IV, “Status of Solar Sail Propulsion: Moving Toward an Interstellar Probe” MFC-426-Paper (2006).
12. G. L. Matloff, “Graphene: the ultimate interstellar solar sail material?” J. British Interplanetary Society 65, 378 (2012).
13. G. Vulpetti, L. Johnson, G.L. Matloff, “Solar Sails. A Novel Approach to Interplanetary Travel,” (Springer, 2015).
14. G. Swartzlander, L. Johnson, B. Betts, Optics and Photonics News 31, 30-37 (2020).
15. R. Y. Kezerashvili, “Space exploration with a solar sail coated by materials that undergo thermal desorption.” Acta Astronautica 117, 231-237 (2015).
16. E. Ancona, R. Y. Kezerashvili. “Extrasolar space exploration by a solar sail accelerated via thermal desorption of coating,” Advances in Space Research 63, 2021 (2019).
17. “Parker Solar Probe,” NASA NP-2018-06-224-GSFC (2018).
18. R. W. Lyman, M. E. Ewing, R. S. Krishnan, D. M. Lester, R. L. McNutt, “Solar Thermal Propulsion for an Interstellar Probe,” AIAA 3377 (2001).
19. L. Alkalai, N. Arora, S. Turyshev, M. Shao, S. Weinstein-Weiss, M. Opher, S. Redfield, “A Vision for Planetary and Exoplanets Science: Exploration of the Interstellar Medium – The Space Between Stars,” IAC-17-D4.4.1x41640, 68th International Astronautical Congress, Adelaide, Australia (2017).
20. K. Nock, “TAU – A Mission to a Thousand Astronomical Units,” paper #AIAA-87-1049 presented at 19th AIAA/DGLR/JSASS International Electric Propulsion Conference, May 11-13, 1987, Colorado Springs, CO (1987).
21. L. Johnson et al., “Electric Sail Propulsion for Exploring Nearby Interstellar Space” https://ntrs.nasa.gov/archive/nasa/casi.ntrs.nasa.gov/20150022344.pdf (2015)
22. G. Marx, “Interstellar Vehicle Propelled By Terrestrial Laser Beam,” Nature 211, 5044 (1966).

23. J. L. Redding, “Interstellar Vehicle propelled by Terrestrial Laser Beam,” Nature 213, 5076 (1967).
24. W.E. Moeckel, “Propulsion by impinging laser beams,” J. of Spacecraft and Rockets 9, 12 (1972).
25. R. Forward “Roundtrip Interstellar Travel Using Laser-Pushed Lightsails,” J. Spacecraft and Rockets 21, 187-195 (1984).
26. G. A. Landis, “Optics and materials considerations for a laser-propelled lightsail”. In: IAF, 40th International Astronautical Congress, Spain (1989).
27. G. A. Landis, “Small laser-propelled interstellar probe”. In: IAF, 46th International Astronautical Congress, Norway. (1995).
28. G. A. Landis. “Advanced Solar-and Laser-pushed Lightsail Concepts”. In: NIAC (1999).
29. G. A. Landis. “Dielectric films for solar and laser-pushed lightsails”. In: AIP Conference Proceedings. 504, 1, AIP (2000).
30. P. Lubin “A Roadmap to Interstellar Flight,” JBIS 69 (2016)
31. K. Parkin “The Breakthrough Starshot System Model” Acta Astronautica 152, 370-384 (2018)
32. F.J. Dyson "Interstellar Transport". Physics Today. 21, 41 (1968)
33. PDF C. R. Williams et al., ‘Realizing “2001: A Space Odyssey”: Piloted Spherical Torus Nuclear Fusion Propulsion’, 2001, 52 pages, NASA Glenn Research Center
34. Borowski, S.K. (1989), “Nuclear Propulsion--AVital Technology for the Exploration of Mars and the Planets Beyond,” NASATechnical Memorandum 101354 (1989)
35. Crawford, I. A. “Interstellar Travel: A Review for Astronomers”. Quarterly Journal of the Royal Astronomical Society. 31: 377–400. (1990).
36. S. Turyshev et al., “Direct Multipixel Imaging and Spectroscopy of an Exoplanet with a Solar Gravity Lens Mission” arXiv:1802.08421. (2020).
37. S.G. Turyshev et al., “Science opportunities with solar sailing smallsats,” Planetary and Space Science 235, 105744 (2023)